IDEA League

Master of Science in Applied Geophysics

Research Thesis

Localization of ocean seismic noise

Olivier F.C. den Ouden

August 31, 2017

Koninklijk Nederlands
Meteorologisch Instituut
Ministerie van Infrastructuur en Milieu

Localization of ocean seismic noise

Master of Science Thesis

for the degree of Master of Science in Applied Geophysics
by

Olivier F.C. den Ouden

August 31, 2017

Je bent hier in de donkere kamer.
Maar nergens ter wereld komt zoveel aan het licht als in een donkere kamer!

W. F. Hermans

IDEA LEAGUE
JOINT MASTER'S IN APPLIED GEOPHYSICS

Delft University of Technology, The Netherlands
ETH Zürich, Switzerland
RWTH Aachen, Germany

Dated: *August 31, 2017*

Supervisor(s):

Prof. Dr. L.G. Evers

Ir. P. Smets

Committee Members:

Prof. Dr. Ir. E.C. Slob (replaces L.G. Evers)

Ir. P. Smets

Prof. Dr. F. Wellmann

Abstract

All over the world a so called oceanic 'hum' can be recorded, dominating the ambient noise field. The hum is generated by nonlinear interaction of ocean surface waves, radiating acoustic signals in the atmosphere and water (named microbaroms), and coupling to the solid earth as microseisms. The hum can be generated by local near-coastal sources and distant deep ocean sources. Deep oceanic generated 'hum' occurs within the range 0.1-0.3 Hz, dominantly around 0.2 Hz. The near-coastal generated 'hum' occurs at higher frequencies. Microseisms are mainly recorded as surface waves corresponding to near coastal activities. These surface waves overwhelm the weaker deep ocean signals, body and surface waves, because they attenuate less due to the shorter travel path. Previous studies are done with individual 3-component sensors, thus spectral data of all kind of microseisms, or for teleseismic distances only. This study of deep ocean microseisms is done by seismic arrays to analyze regional microseisms. Arrays provide more information about the microseisms by applying beamforming. This enables an improved localization of the source area, in specific near coastal activity or deep ocean generated. To validate the observed results a comparison with the numerical simulated source area is be made. Denote that the use of seismic arrays requires verification on the performance of arrays due to local conditions (sensitivity variances) to find possible deviations regarding the back azimuth. It is shown that, using classical beamforming, the recordings are dominated by near coastal surface waves. Applying adaptive beamforming using multiple signal classification, also other events become visible in the f-k spectrum. Due to this method an improved deep ocean source area is obtained. This observed source area agrees with the simulated source area. Improving the localization requires to define array correction factors.

Keywords: Ambient noise, Microseisms, Phase distinction, Seismic arrays, Beamforming, Localization, Seismic array corrections, Numerical source modeling.

Acknowledgements

I would like to express my gratitude to both my supervisors Läslo Evers and Pieter Smets for their continuous support, motivation and enthusiasm at all stages in my masters thesis. Also many thanks to my colleagues at the KNMI, always available for questions and a critical view, in particular Jelle.

Besides the people that were closely related to this thesis, I also want to thank all the different professors that taught me through the years, at all different universities.

Also many thanks to all my friends from; Delft - Vienna - Zürich - Aachen, and my friends from sailing. Without you guys my period of studying would not have been so much fun.

Finally, I want to thank my family. My dad for his sharp technical view on everything. Mom for being my social mirror, showing me the goods and the bads and for being my all time advice machine. And Carly, keeping me updated with the latest trends and being the one that asked the most difficult questions the easiest way.

KNMI / Delft University of Technology
August 31, 2017

Olivier F.C. den Ouden

Table of Contents

List of Figures

List of Tables

Acronyms

KNMI Royal Netherlands Meteorological Institute

NORSAR Norwegian Seismic Array

CTBT Comprehensive Nuclear-Test-Ban Treaty

ECWMF European Centre for Medium-Range Weather Forecasts

WAM WAve Model

P-Waves Primary (Compressional) body waves

S-Waves Secondary (Shear) body waves

SNR Signal to Noise ratio

SASC Slowness Azimuth Static Corrections

BHZ Broadband sensor

HHZ High sampling sensor

SHZ Short Sampling sensor

Chapter 1

Introduction

All over the world a so called oceanic 'hum' can be recorded. This hum can be recorded as an acoustic signal in the atmosphere and water (named microbaroms), and as a seismic signal in the solid earth (named microseisms). The hum can be generated by local near-coastal sources and distant deep ocean sources.

Besides the hum there are many other events that can be recorded. Think of earthquakes, volcanic eruptions or nuclear tests. All these events have unique recordings and are impulsive, what makes them easy to detect. The hum is a continuous signal and will always overwhelm the other events, thus be visible.

Due to the fact that the hum is always detectable it is called 'ambient noise'. The oceanic hum is generated by the nonlinear interaction of two ocean waves, of the same period but of opposite direction [Longuet-Higgins, 1950]. Due to this interaction, acoustic energy is radiated into the atmosphere and through the water column (generating microbaroms). Resonance of the water column results in continuous oscillations of the earth's ground results in oceanic microseisms. Deep oceanic 'hum' occurs within the range 0.1-0.3 Hz, dominantly around 0.2 Hz [Posmentier, 1967]. The near-coastal generated 'hum' occurs at higher frequencies.

Because of their low frequency, and thus large wavelength, microseisms can travel further than regular seismic signals because they are less attenuated, what makes them detectable all over the world.

These microseisms can be generated in the deep ocean and due to near coastal activities. According to [Shearer, 2010], there are three ranges of seismic waves.

- Local seismology, occurring around 200km from source. The focus is only on direct body waves.
- Regional seismology, for waveforms between 200/2000km from source. In this region, the same phases are recorded but the surface waves become more apparent and easier to observe.

- Global seismology, distances beyond 2000 km from source. In this region, the waveforms are called teleseisms. Teleseisms body waves travel more through the mantle and core of the earth. For shallow surface sources, surface waves are also still detectable with the highest amplitude.

In addition to the specific frequencies of the microseisms, there is also a phase aspect within the microseisms. A signal exists of different phases. The two main phases are the body and surface waves.

Body waves are seismic waves that travel through the interior of the earth. As they travel deep into the earth, body waves will travel along paths that are controlled by material properties in terms of density and stiffness. Density and stiffness vary with temperature, composition and material phase. There are two main types of body waves; P- and S-waves.

- P-waves, or compressional waves are longitudinal pressure waves. The particles move in the direction of propagation. Because of this, P-waves are the fastest waves and can travel through each kind of material phase, fluid or solid. Due to high speed of propagation, P-waves are always recorded first by the recorders (primary waves).

- S-waves, or Shear waves have a particle motion perpendicular to the propagation direction. Therefore, the propagation depends on a shear force in the medium to propagate. The shear waves are also known as fast waves but slower than the P-waves, see Figure 1-1. In case of liquid, shear stress between the particles is low, hence S-waves do not propagate.

In contrast with body waves, surface waves travel along the earths surface. Besides the difference in paths, surface waves also have a smaller velocity than body waves. Surface waves can be divided in two main types of waves, Rayleigh waves and Love waves.

- Rayleigh waves are the so-called ground roll waves. These surface waves travel in the same manner as ocean waves over water do, ripples with motion, but they travel over the surface of the crust. Rayleigh waves have both the longitudinal and transverse motion, see Figure 1-1. Besides the Rayleigh waves also Love waves can be identified out of the surface waves. The Love waves are horizontal shear waves at the surface.

Often microseisms are detected as surface waves. They overwhelm the also generated body waves. Problem with these surface waves is that they can be generated in the deep ocean but overwhelmed by other microseismic surface waves. These 'new' generated surface waves come from near coastal activities, due to there smaller travel path they lost less energy what makes it possible to overwhelm the weakened deep ocean signals.

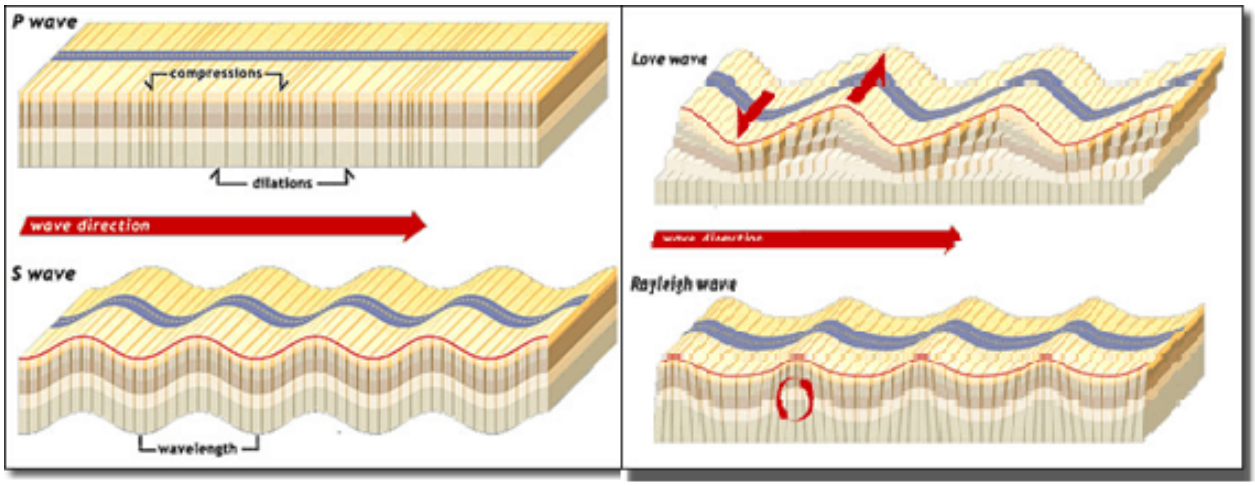

Figure 1-1: Different phases. Left; Body waves, Right; Surface waves.

Oceanic ambient noise sources can also be simulated, [Longuet-Higgins, 1950], for the solid earth ([Kedar et al., 2008, Ardhuin and Stutzmann, 2010, Obrebski et al., 2013]) and atmosphere ([Brekovskikh, 1973, Waxler and Gilbert, 2006]) by use of an ocean surface wave model. Out of these studies it becomes clear that oceanic ambient noise can be modeled well. Remark for that, for the solid earth, numerical simulations are mainly based on spectra, [Kedar et al., 2008, Ardhuin and Stutzmann, 2010, Obrebski et al., 2013]. [Kedar et al., 2008] compared the numerical source area with the are denoted by seismic observations. Although Kedar's studies shows good results. a more detailed approach is done in this research.

This study will focus on detecting and localizing these microseisms by use of seismic arrays instead of 3-component stations. The use of arrays makes it possible to apply beamforming. Out of this beamforming more information about the recorded microseisms is obtained, which is not possible using 3-component stations. By use of this new information a better comparison can be done for each different phase regarding the source area, near coastal activity or deep ocean generated. To validate the observed results a comparison with the numerical source area will be made. This will give an idea about the coupling between ocean surface energy and the bathymetry, and thus the are where deep ocean ambient noise arises.

In this study, seismic arrays are used part of the International Monitoring System (IMS) for the verification of the Comprehensive Nuclear-Test-Ban Treaty (CTBT). The CTBT bans nuclear explosions by everyone, everywhere: on the Earth's surface, in the atmosphere, underwater and underground. Their sensors are placed all over the world to keep an eye on all nations, with respect to the Nuclear-Test-Ban Treaty. But, besides the check on nuclear activities, it can also be used to detect other events. [Dahlman et al., 2009]

Besides the knowledge about the microseismic source location, this study is also interesting for the CTBT. By having a better knowledge about the noise level, and regions, it becomes easier to detect a signal, like a nuclear test.

Another interesting feature of this study is the verification of the seismic arrays. By use of known events (earthquakes) all arrays are analyzed. This analysis is done to verify the performance of the arrays based on local conditions (sensitivity variances). The goal is to

find possible deviations regarding the back azimuth. By knowing these flaws, some corrections can be moot and applied.

The outline of this thesis is as follows. First, the theory is provided Chapter 2. The required background information about microseisms, arrays and processing.

Next, the array characteristics are analyzed by studying earthquakes in Chapter 3. In Chapter 4, array deviations are discussed and analyzed. This gives an idea about the origin of the founded flaws and recommendations for corrections.

Chapter 5 will focus on ambient noise. Deep ocean microseismic source regions are studied by use of observed data and simulated data. These two approaches are compared and discussed.

Chapter 2

Theory

2-1 Receivers / Array

Two different methods are widely used to record seismic recordings. The first method is by using a three component sensor. This sensor is places individually at a certain place. The sensor records in the x, y and z direction. By knowing the difference in arrival time, phase between different 3-component sensors, an azimuth and trace velocity of the event can be calculated. The other method is by recording seismic events with an array, a series of (single or multiple component) sensors at a certain place. An array gives an azimuth and trace velocity after some calculations (beamforming). This calculation is more accurate and gives more information about the event.

Array design

To make sure a good recording of the microseisms, and so the event/source, it is necessary to not have aliasing. Aliasing can occur due to time-sampling rate, Nyquist, and because of spatial- sampling of the recordings. When a source cannot be uniquely identified, assuming there is no aliasing due to the time-sampling, its because of sample aliasing. In case of spatial sampling multiple solution exist for the apparent speed and back azimuth, what is not preferable. [Evers, 2008]

To check for aliasing and the sensitivity of an array is, the array response is observed. Assumed is that signals travel as a plane wave over the array. The plane wave is expressed as;

$$f(\overrightarrow{r}, t) = e^{i(\overrightarrow{k} \cdot \overrightarrow{r} - \omega t)} \tag{2-1}$$

Where ω is the angular frequency, t the travel time, r the receiver position and k the wavenumber. To express the array response in terms of slowness, Equation 2-1 can be rewritten by use of $p = k/\omega$, what results in;

$$f(\vec{r}, t) = e^{i\omega(\vec{p}\,\vec{r} - t)} \tag{2-2}$$

To have a good array response the sensors within an array are positioned in such a way that R(ω,p), array response, approximates a delta function around a desired/initial slowness, p_0.[Lacoss et al., 1969]. The number of sensors and inter-sensor distances control the amount of spatial aliasing.

$$R(\omega, \vec{p}) = \left| \frac{1}{N} \sum_{n=1}^{N} e^{-i\omega[(\vec{p} - \vec{p_0})\vec{r_n}]} \right| \tag{2-3}$$

N is the number of stations.

In Figure 2-1 one can see the array responses of three different surveys. In all three cases, the main lobe is positioned in the middle of the p_x-p_y plot, unregarded the frequency. The main lobe has a circular shape what indicates the array has no preferred orientation, thus a vertical incidence angle with zero delay between the array elements can be assumed.

Besides the main lobe, one can also observe other lobes, so called side lobes. In this easy example its straight forward which lobe is the main lobe, because a plane wave from above the array is used. When dealing with a bigger survey, or more data, it can cause problems. So, it is important to see how to eliminated these side lobes. One way is changing the survey setup, by increasing inter-sensor distance and angles the side lobes move away from the main lobe. The inter-sensor distance plays a crucial role in reaching the optimal array, with the best response.

The general array design criteria are given by [Evers, 2008]:

- The main lobe has a circular shape. This means the array is equally sensitive to all arrivals, independent of its back azimuth.
- The main lobe is as small as possible. The inclination and back azimuth will be resolved with the maximum accuracy since energy is minimal smeared out.
- Side lobes are small in amplitude. Most energy is present in the main lobe, enabling maximum resolution and avoiding spatial aliasing.
- Side lobes are as far away from the main lobe as possible. The main lobe will be unambiguously identified and spatial aliasing will be avoided.

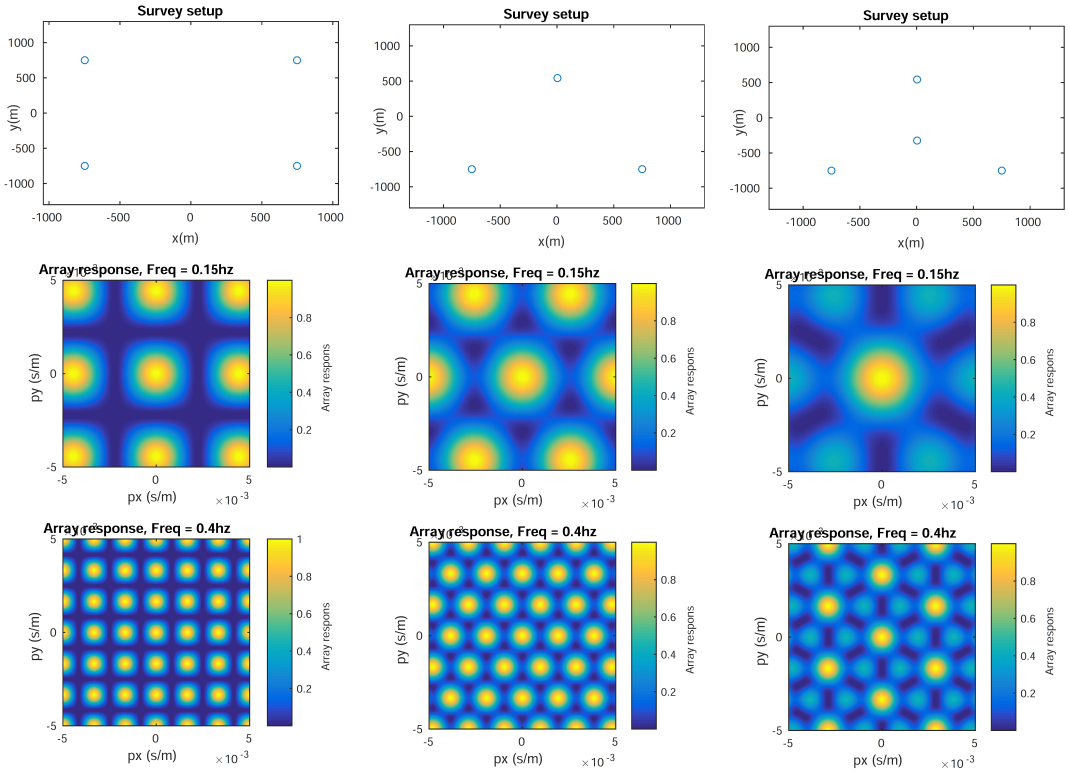

Figure 2-1: Different survey setups and their array response. p_0=0.

Array response

Besides the array design also the used instruments/receivers influence the sensitivity. There are two types of sensors that can be used. Either a vertical component sensor or a three component sensor. The components are divided in Depth(Z-), North(N-) and East(E-). Another difference in receivers is the channel type, the main types of sensors are listed below in table 1.1 with their specifications;

MSEED description

Channel	Description
EHZ/EHN/EHE	Short period recording, 100 sps
BHZ/BHN/BHE	Broad band recording, 20 sps
LHZ/LHN/LHE	Long period recording, 1 sps

Table 2-1: MSEED channels and description from [Ahern et al., 2007]

Each sensor has its own response (sensitivity for a given frequency), based on a transfer function of the instrument and data logger. This results in an instrument sensitivity range. To obtain the true signal one needs to correct for this instrument response. In the flat band nothing additional is required (besides a gain shift) to compare different instruments. Once in the corners, the actual signal is retrieved by removing the instrument (or entire system) response.

In the Figure 2-2 one can see when the different channel types have their best recording period. In this figure, it becomes clear that a broad band receiver is the most ideal receiver when dealing with microseisms, the largest 'flat' band. Only disadvantage of the broad band receivers is that they are more expensive compared to the other channel types.

Figure 2-2 also shows a broadband response of a GERESS GEC BHZ station. In here one can observe that when dealing with frequencies outside the sensitivity range there is a phase and amplitude transformation of the signals, see Appendix E for the station response per used array of this studies.

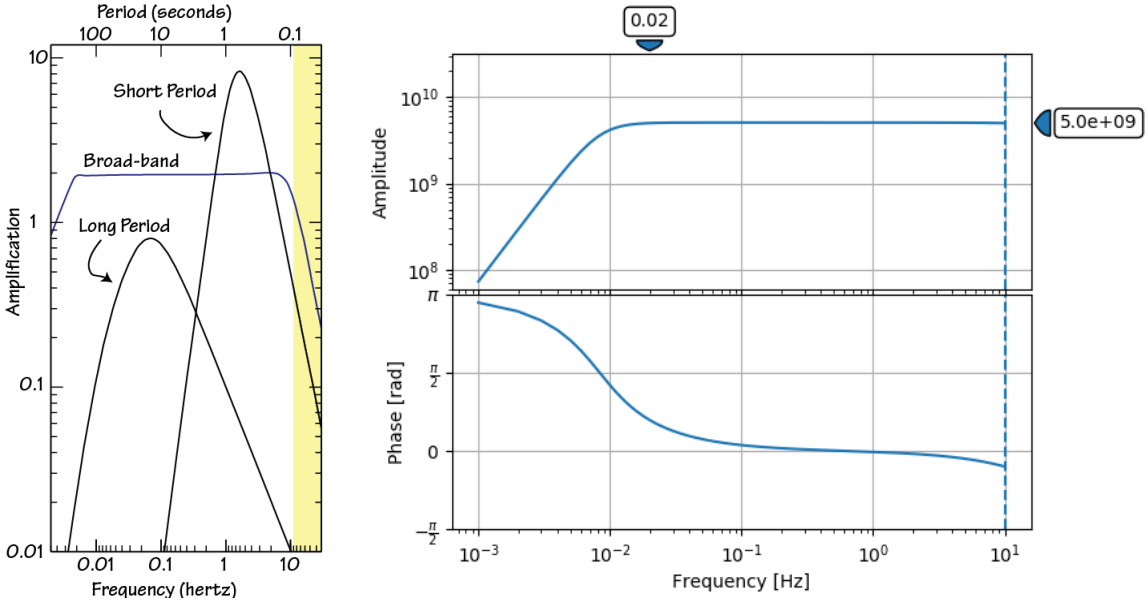

Figure 2-2: Array response. Left; Difference of array response dealing with different channel types. Right; GERESS GEC BHZ station response.

When the array exists of different types of sensors, the signals first need to be corrected by removing the instrument response, otherwise the signal will be transformed what can cause problems by applying a Fourier transformation. When dealing with an array exiting of the same type of instruments, a response correction is not needed when the true amplitudes of the best beam (or for interferometry) are not required.

2-2 Trace velocity

As already mentioned before, there are different phases within a signal. The arrays record every signal phase. Between this different phases is, besides the way of propagation, a large velocity difference. In Figure 2-3 one can deduct the difference in velocity of different types of body waves in different sections of the earth.

From Figure 2-3 one can deduct that body waves have different velocities due to the internal structure of the earth. Surface waves are influenced by difference in velocity due to different earth layers in the crust.

Although the signals have a certain velocity, this is often not correct measured at the array. At the array a so called trace velocity is measured, the apparent velocity of the signal traveling over a recording array. The trace velocity relates to the true velocity, see 2-4.

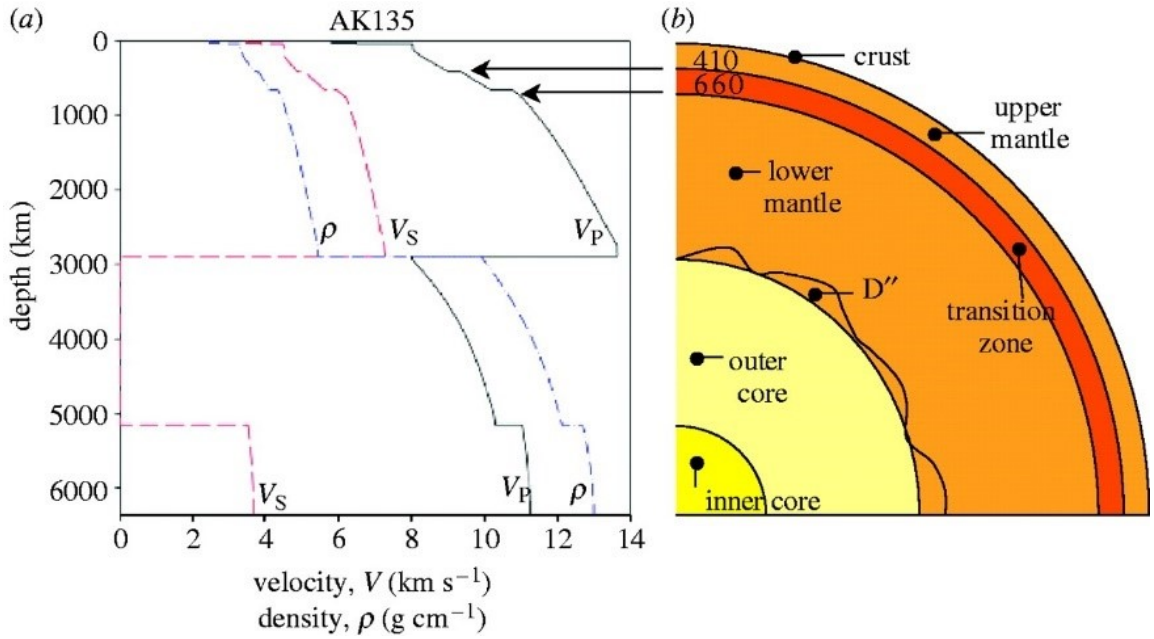

Figure 2-3: AK135 Velocity model and a cross section of the Earth. In the velocity model one can see the velocity curve of the P- and S-waves plus the density curve. Something noticeable is the velocity, to zero, of the S-waves. This is because the outer core exists of liquid material, no shear is possible.

$$C_{trace} = \frac{C_{eff}}{\cos(\theta)} \tag{2-4}$$

When compressional and surface waves move away from sources, there is already a big difference in true velocity. When the signal is observed at an array, this difference in velocity will become even bigger. Compressional waves come from below the array, approaching under an inclination angle. The bigger the inclination angle, the higher the apparent/trace velocity. This while the surface wave will always come in parallel to the array, what means that the trace velocity ≈ true velocity.

[Gerstoft et al., 2008] and [Huang et al., 2013] discuss the paths of body waves in the earth. In Figure 2-4 one can obtain the travel paths of compressional body waves, direct and one reflected phase, plus the slowness plot that belongs to the phases they discussed in their research.

As shown in Figure 2-4, they used the travel paths to come up with time-distance (velocity) curves for different angles (arc lengths). The velocity curve is nonlinear. By an increasing arc length, the velocity increases ≈ slowness decreases.

Out of [Huang et al., 2013] one can conclude that, besides the inclination angle, also the wave path contributes to a faster propagation of body waves.

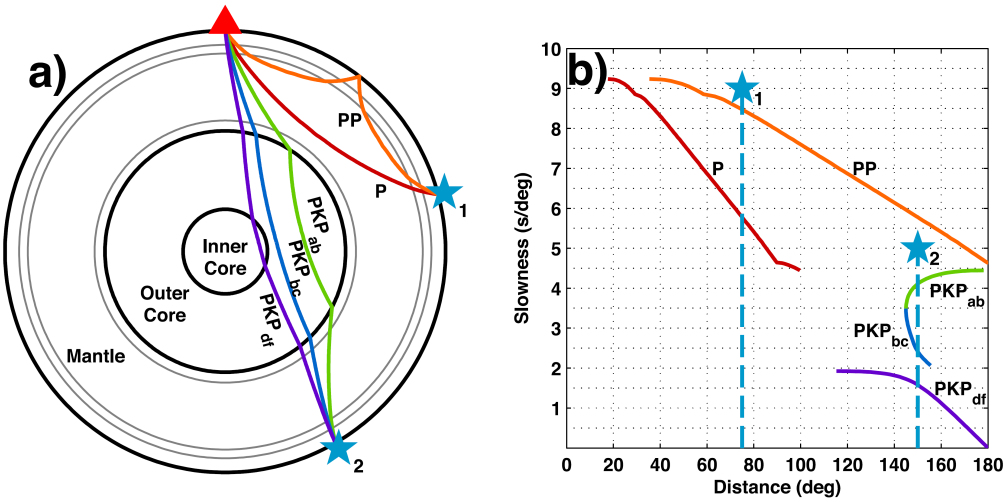

Figure 2-4: a.) Direct compressional body wave paths through Earth. b.) Slowness versus distance plot. [Euler et al., 2014].

2-3 Attenuation

As [Huang et al., 2013] showed, theoretically at any position at the earth receivers can record body waves. Often signals are distinguished form noise because signals have a higher amplitude compared with the noise.

When a signal is generated, it has an initial amount of energy. In case of a lossless medium, the amount of energy from start, E0, is equal to recorded energy, E. But since the Earth is not a lossless medium this is not the case. [Bugeja, 2011]. Between source and receiver the seismic waves are attenuated. This attenuation can be seen as a simple equation;

$$\text{Attenuation} = \text{Geometrical spreading} + \text{Scattering} + \text{Oscillation} \tag{2-5}$$

Geometrical spreading

The biggest decay of amplitude is due to geometrical spreading. The initial energy that is released, and causes the signal, will spread over an ever-increasing area and thus the intensity of energy decreases with distance. [Bugeja, 2011].

The difference in geometrical spreading, between surface and body waves is indicated by the path of traveling. Surface waves follow the earths surface, the spreading of their energy is only in the crust while the energy of body waves is spread over the whole earth.

$$\text{Decay factor surface waves} = \frac{1}{r} \tag{2-6}$$

$$\text{Decay factor body waves} = \frac{1}{r^2} \tag{2-7}$$

Equations 2-6 and 2-7 show that over an equal travel distance r, the body waves have lost more energy than the surface waves. Resulting in a higher energy/amplitude of the surface waves and so a better visibility in the recordings.

Scattering

Besides geometrical spreading, scattering also needs to be considered. When a seismic wave encounters a boundary of different impedances a part of the energy will transmit into the second layer while another part will reflect at this boundary. The more boundaries crossed, the more the wave is scattered and thus energy decays.

The amount of reflection versus transmission depends on the difference in impedance, [Dana, 1944] and [Zoeppritz and ERDBEBENWELLEN, 1919]. Observing the travel path of body waves large difference in velocity occur. This results in large differences in impedances and so in strong decays of signal energy.

Comparing this with the surface wave path, in the crust, one can conclude that the differences in impedance of crust layers is smaller as the impedance difference of the earth interior.

Oscillation

Another phenomenon, is attenuation due to oscillations. In every oscillation, a certain amount of energy (amplitude) is lost. [Bugeja, 2011], Equation 2-8. Attenuation due to oscillation is an approximation of energy absorption by the medium expressed in loss per time, oscillation.

$$A(x) = A_0 e^{\frac{-\omega x}{2cQ}} \tag{2-8}$$

Where A is the amplitude/energy after a certain amount of oscillations, A_0 the initial amplitude, omega the angular frequency, x the distance of propagation, c the velocity of the wave and Q the attenuation factor.

The Q factor is often defined by a model, where each earth layer has a different value. Although this is an essential part of the attenuation, there is not much information about it. In [Gualtieri et al., 2013] they describe the Q model and it effect for surface wave. Not much information is provided for body waves, [Kee,].

Considered attenuation

Since this research is dealing with microseisms, the wave frequencies of interest are between 0.1 and 0.3Hz. Because of these low frequencies, and thus large wavelength, microseisms can travel further than regular seismic signals because they are less attenuated, what makes microseismic body waves detectable over the whole world.

Due to the attenuation factors, this research will mainly focus on direct arrivals of all different microseismic phases. This because refractions/reflections lose to much energy due to transmission and reflection and as described before the waves already lost a big amount of energy due to the large travel distances.

Dealing with only direct waves, means dealing with a so called shadow zone for body waves. This shadow zone is the region where no direct body wave arrivals occur. For the compressional body waves this is the area between 95 and 140 degrees earth degrees away from source. For the direct S-waves this is the area after 95degrees arc length. This because there are no direct S waves coming through the earths core, while the earth core is liquid, see Figure 2-3.

2-4 Array processing

In section 2-1 the plane wave approached the array from above. In a real scenario, this is not the case. While recording the stations record all kinds of signals from all different directions. Most these records can be called ambient noise with no, or a small fraction of, coherence. In case of an event the recordings will have a mutual high coherence. This high coherence indicates the event. When a coherence is spotted, the direction(back azimuth) and velocity (trace velocity) of the signal can be determined and so, by use of multiple arrays, the source location.

Data check and filtering

The first step is checking the data. Out of this observation one can detect the frequencies of interest, if there are gaps in the recording, if the signal is constant, if there were earthquakes and so on. It is the first quality check of the data.

Having this knowledge, a filter can be applied. For example, a second order Butterworth bandpass. This filter removes any DC offset or linear trend, necessary because when transforming the signal to the frequency domain, by Fourier transformation, the data would be dominated by low-frequency components.

Window processing

After filtering, the data is split into overlapping time segments, bins. This is done to make sure no signal, event, is missed.

For every bin the goal is to find the highest coherence between the recordings of different stations within the array. To do so, several slownesss [p] are defined, with x- [p_x] and y-component slowness[p_y]. This slowness p can be rewritten into a $\triangle$t, time shift, in the time domain or a $\overrightarrow{k}$ value, phase shift, in the frequency domain.

Coherence analysis, Fisher

By use of this $\triangle$ t or $\overrightarrow{k}$ the binned data is shifted. For this shifted data the Fisher ratio between all station signals is calculated. The Fisher ratio is the indication of coherence between the shifted signals of the stations.

Beam forming, best beam method

For every bin a specific combination of p_x and p_y results in the best shift to have the highest Fisher ratio. By use of this highest Fisher ratio per bin, the velocity and back azimuth can be calculated.

For each bin the best beam is found this way. The best beam, is the sum of all time aligned traces for the slowness at the maximum detector value. Incoherent noise will cancel out and the signal will be enhanced. The apparent velocity and back azimuth are known at the maximum Fisher ratio, the event is characterized. [Evers, 2008]

Best Beam forming in time domain

The recording is split into several bins. Let each bin consist of T recordings, samples/data points, and N stations. By time shifting the bins, for each sensor of the array, the Fisher ratio can be calculated;

$$F = \frac{T(N-1)}{N(T-1)} \frac{\sum_{t=1}^{T}(\sum_{n=1}^{N} x_{nt})^2 - \frac{1}{T}(\sum_{t=1}^{T}\sum_{n=1}^{N} x_{nt})^2}{\sum_{t=1}^{T}\sum_{n=1}^{N}(x_{nt})^2 - \frac{1}{N}\sum_{t=1}^{T}(\sum_{n=1}^{N} x_{nt})^2} \tag{2-9}$$

Over the whole slowness range different time shifts per bin are found. For all time shifts the Fisher ratio is calculated. The highest Fisher ratio indicates the highest coherence, and so the possible detection of an event.

From this maximum Fisher ratio, the direction and trace velocity of the event are obtained.

Best Beam forming in frequency domain

Time domain recordings are transformed to the frequency domain by use of the Fourier transform. The shift is a phase shift and obtained by knowing the wavenumber.

$$\overrightarrow{p} = \overrightarrow{k}/\omega \tag{2-10}$$

Where $\vec{k}$ is the wavenumber and ω the angular frequency. The total amount of energy in the selected recordings yields.

$$P_T(\omega) = \frac{1}{N}\sum_{n=1}^{N} |G(\omega, \overrightarrow{r_n})|^2 \tag{2-11}$$

Where G is the Fourier transform of the recordings and N the number of stations. The amount of signal energy is given by:

$$P_S(\omega, \overrightarrow{k}) = |\frac{1}{N}\sum_{n=1}^{N} G(\omega, \overrightarrow{r_n}) e^{-i\overrightarrow{k}\cdot\overrightarrow{r_n}}|^2 \tag{2-12}$$

Out of the two energy terms the Signal to Noise ratio, SNR, is calculated:

$$F(\omega, \overrightarrow{k}) = \frac{P_S(\omega, \overrightarrow{k})}{P_T(\omega) - P_S(\omega, \overrightarrow{k})}(N-1) \tag{2-13}$$

Like done in the time domain, for each phase shift the fisher ratio is calculated. Out of this the highest Fisher ratio is stored, from where trace velocity and back azimuth is determined of the event.

Beam forming, Barlett beam and Clean

The second beamforming method is the Barlett beamforming, (Barlett 1948), and used in [Gal et al., 2016]. In case of Barlett beamforming the cross power spectral density is given as;

$$C(f) = \frac{1}{L}\sum_{l=1}^{L} X_l(f)X_l^{\dagger}(f) \tag{2-14}$$

$X_l(f)$ denotes the Fourier transform of the l-th snapshot, † is the conjugate transpose, f the frequency and L the number of snapshots. The phase information for the wave fields at each seismic sensor is presented in the cross spectral matrix C. The power output of the beamforming is;

$$P(W) = w^{\dagger}C(f)w \tag{2-15}$$

Here w is used as weight factor. The weight factor is obtained by maximizing the output power of the beamforming;

$$w_B = \frac{a(k)}{\sqrt{a^{\dagger}(k)a(k)}} \tag{2-16}$$

With a(k) as steering vector and k the wavenumber. this leads to the power spectrum;

$$P_B(k) = w_B^{\dagger}(k)C(f)w_B(k) \tag{2-17}$$

The advantage of this beamforming is that after the beamforming process an adaptive beamforming using multiple signal classification is applied. The idea of this "clean" factor is that phase information associated with the strongest source directly is removed from the cross spectral matrix. Hence mitigating edge effects for beamforming results that suffer from strong side lobes.

The cleaned beamforming, C_{clean} can be formulated by removing iteratively a fraction of the dominant source power of the original $P_{B,max}$ from the original cross spectral matrix;

$$C_{clean}^{i+1} = C^i - \phi P_{B,max}^i w_{max} w_{max}^{\dagger} \tag{2-18}$$

ϕ is the parameters that determines the fraction of removed power, w_{max} the normalized steering vector and C^i the original cross spectral matrix.

Out of this cleaned matrix an clean power spectrum can be generated;

$$P_{clean}(k) = \sum_{i}^{M} \phi P^i_{B,max} \tag{2-19}$$

Where M is the number of iterations and $\phi P^i_{B,max}$ the amount of reduced power. This results in a final 'cleaned' beamforming spectrum;

$$P_{final}(k) = w^{\dagger}_B(k) C^M_{clean}(f) w_B(k) + P_{clean}(k) \tag{2-20}$$

By use of this final spectrum a more detailed analysis can be done. The best beam beamforming selects the point, p_x and p_y, with the highest coherence and removes the other information. This cleaned spectrum shows, besides the highest coherence, also other coherence points. By use of this 'clean beamforming' more information about the recordings can be obtained, regarding different phases.

2-5 Source localization

From the processing, we obtained the apparent velocity and back azimuth of an event for a specific array. Knowing the velocity and azimuth of an event does not mean automatically that you know the source location of the event.

To localize the source, it is necessary to have at least two arrays that recorded the event. From both arrays a velocity and azimuth of the event can be obtained. By use of cross bearing the location of the source can be determined.

Cross bearing

To calculate the location, first some mathematical background will be showed and explained. From an array A one knows the position of the array, PA position vector, and obtained the velocity in vector form, DA direction vector. This information is also given for array B.

$$P_A = \begin{pmatrix} X_A \\ Y_A \end{pmatrix}, D_A = \begin{pmatrix} V_x \\ V_y \end{pmatrix} \tag{2-21}$$

To determine the position of the source one needs to find out where the direction vectors of array A and B will cross.

$$r_A = P_A + D_A \cdot t_A \tag{2-22}$$

$$r_B = P_B + D_B \cdot t_B \tag{2-23}$$

Where r_A is the cross point calculated by use of array A and r_B for array B. t is the time of traveling, the unknown in Equation 2-22 and 2-23.

In case of a cross bearing, one is interested in the location where r_A and r_B intersect, $r_A = r_B$.

$$P_A + D_A \cdot t_A = P_B + D_B \cdot t_B \tag{2-24}$$

$$P_A - P_B = c \tag{2-25}$$

Where c should agree:

$$c_x = t_B \cdot D_{Bx} - t_A \cdot D_{AX} \tag{2-26}$$

$$c_y = t_B \cdot D_{By} - t_A \cdot D_{Ay} \tag{2-27}$$

Rewriting gives;

$$t_A = \frac{c_y \cdot D_{Bx} - c_x \cdot D_{By}}{D_{AX} \cdot D_{By} - D_{Ay} \cdot D_{Bx}} \tag{2-28}$$

By knowing the t for each array, and the array uncertainty, a good estimation of the source location can be done.

$$\begin{pmatrix} P_{Ax}[m] \\ P_{Ay}[m] \end{pmatrix} + \begin{pmatrix} D_{Ax}[\frac{m}{s}] \\ D_{Ay}[\frac{m}{s}] \end{pmatrix} \cdot t_A[s] = \begin{pmatrix} Source_x[m] \\ Source_y[m] \end{pmatrix} \tag{2-29}$$

Combining more arrays will result in a more accurate source location.

Density ellipse

By calculating the cross-bearing location of all available arrays with each other, one gets a lot of different source locations from each individual cross bearing. To get a measure for the accuracy of the source location, an ellipse is drawn between the two cross bearing location points with the biggest distance between each other.

To get a good idea where in this ellipse the true source location is, a density function is applied within the ellipse. A high density, somewhere in the ellipse, indicates a region with a lot of cross-bearing locations.

Sine location

Besides the density ellipse there is also the option to calculate the Sine location. The idea of this source location is to weight each cross-bearing location by the angle between the two crossing vectors at the location. From this angle the Sine function is taken to weight the given source location.

This Sine location is introduced because when two arrays are have a small angle between there back azimuth directions a 1 degree azimuth error can lead to an enormous difference in cross bearing location.

When dealing with a 90° angle, between the two drawback vectors, the weight of the outcome, source location, is higher as when the angle is 10degrees.

For example, if an event occurs in Italy and is recorded by arrays in Germany and Norway, their angle range from event is almost the same. When one of the arrays have an error of around 1 degree the cross-bearing location will be somewhere in Africa instead of Italy. This error will be smaller when dealing with an array from Norway and Spain, their back azimuth directions differ a lot what will lead to a more accurate source location.

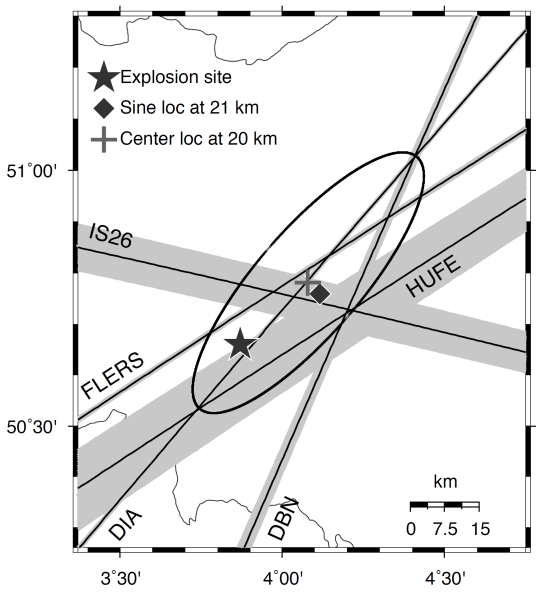

Figure 2-5: Example of cross-bearing ellipse. The black solid lines indicate different drawback vectors from arrays to source. The ellipse is drawn between the two cross-bearing positions most separated from each other. The star indicates the true source location, plus sign the center of the ellipse and the diamond the Sine location calculated from all cross-bearing locations. [Evers, 2008]

2-6 Numerical source modeling

Numerical modeling is used to verify the observed source location. Calculating the numerical source location, source spectrum, starts by calculating the energy spectrum of interacting ocean waves, the Hasselmann integral [Hasselmann, 1963]. Interacting ocean waves, e.g. swell and marine storms, generate standing waves which radiate acoustic energy at double the ocean wave, [Longuet-Higgins, 1950]. Deep ocean microseisms occur within the range 0.1-0.3Hz, dominantly around 0.2Hz [Posmentier, 1967].

[Hasselmann, 1963] related an ocean wave-wave interaction to the directional wave spectra. This integral indicates the wave-wave interaction intensity. From other studies, [Willis et al., 2004]/[Hetzer et al., 2010]/[Landes et al., 2012]/[Donn and Rind, 1972] , it became clear that these wave-wave interactions transmit energy into the atmosphere and ocean, Figure 2-6. These studies focused on wave-wave energy in the atmosphere and showed a good correlation between observed, by use of microbaroms in the atmosphere, and numerical source location.

$$\psi(T) = \int_0^{2\pi} F(T,\theta)F(T,\theta+\pi)d\theta \tag{2-30}$$

ψ is the Hasselmann wave-wave interaction, F us the directional spectral density function depending of the period, T, and direction, θ, of the ocean waves.The first spectral density function corresponds to a certain ocean wave with period and direction, where the second spectral density function corresponds to an ocean wave with same condition but with opposite direction. This ansatz results in a frequency that is double the ocean surface wave frequency. According to several studies ([Kedar et al., 2008],[Ardhuin and Stutzmann, 2010], [Obrebski et al., 2013]), microseisms are generated in regions where the wave-wave intensity is high. The wave-wave interaction intensity is related to several other ocean energy terms, Figure 2-7. Like the significant wave height, H_s.

$$H_s = 4\sqrt{\int_0^{\infty}\int_0^{2\pi} F(T,\theta)d\theta dT} \tag{2-31}$$

[Kedar et al., 2008] implemented the theory of [Longuet-Higgins, 1950] to estimate the ground displacement caused by wave-wave interaction (Figure 2-7).

$$\bar{\delta}(\omega)^2 \simeq 64\pi\omega^2 \sum_i (\wedge\psi(T))\rho^2\bar{W}^2 \tag{2-32}$$

Where $\wedge$ represents the source area, ρ is the density of the medium (which is constant assuming a homogeneous crust). W corresponds to the water-solid response to pressure oscillations caused by the ocean surface wave-wave interaction. For a local source response W yields;

$$\bar{W}(2\omega) = \frac{\omega^2}{\rho\beta^{\frac{5}{2}}}\left[\sum_{m=1}^{N} c_m^2\right]^{\frac{1}{2}} \tag{2-33}$$

[Longuet-Higgins, 1950] defined c_m, resonance/coupling coefficient, as a function of $[\sigma h/\beta]$. Which makes c dependent on ocean bathemetry as well ocean wave frequency and shear velocity.

Although, by having a closer look at the implementations of [Kedar et al., 2008], some side notes are needed. The bathemetry is maybe not used correctly. In Kedar and Longuet-Higgins they apply this coupling factor. This factor is a function of the water depth and the shear velocity. Out of [Ardhuin and Stutzmann, 2010], and personal communication with [Smets,], it becomes clear that the shear velocity is not used correct in this case. Kedar uses the bedrock shear velocity as resonance velocity for the water column, while this needs to be the water-sound velocity to obtain the resonance and so the ground displacement.

Another point of discussion is the accuracy of the numerical source location/coupling location. Kedar shows a lot of spectra, with unknown or random Q values.

In this research, the coupling of energy from the ocean into the solid earth using the theory of Longuet-Higgens 1950 is evaluated. To do, CTBT sensors are used to locate source areas. It is essential that the observed data comes from the deep ocean, this needs to be validated first. Interesting is to see how these observations link with the numerical source areas.

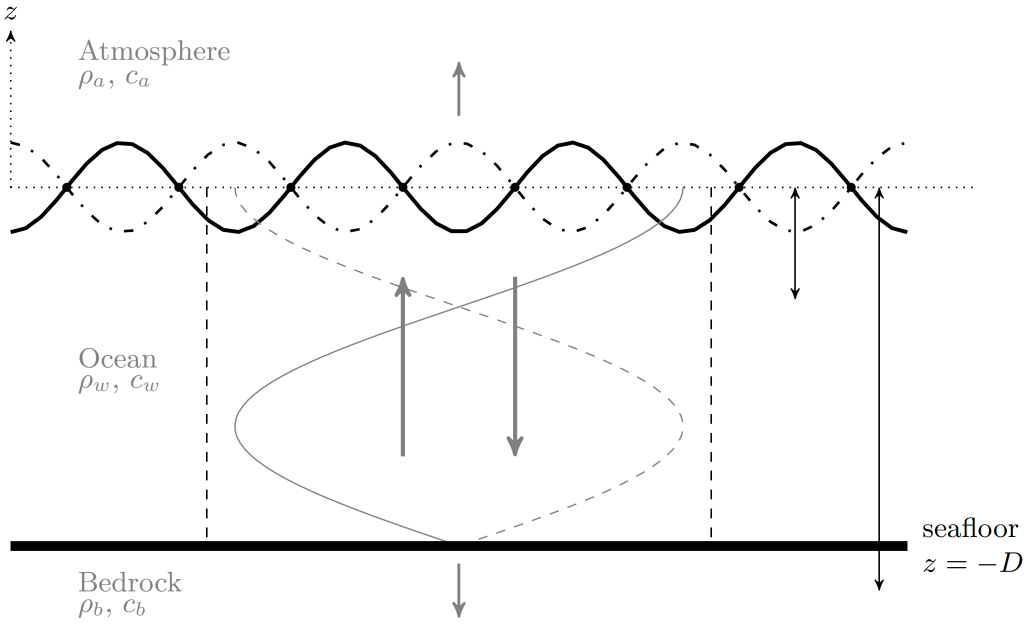

Figure 2-6: Ocean-wave model. Ocean waves, same period but different direction, interact. By interacting energy is coupled to the atmosphere, resulting in acoustic signals (microbaroms), and into the ocean. Due to water resonance, the energy oscillates towards the sea floor where the energy coupled resulting in microseisms. From [Smets,]

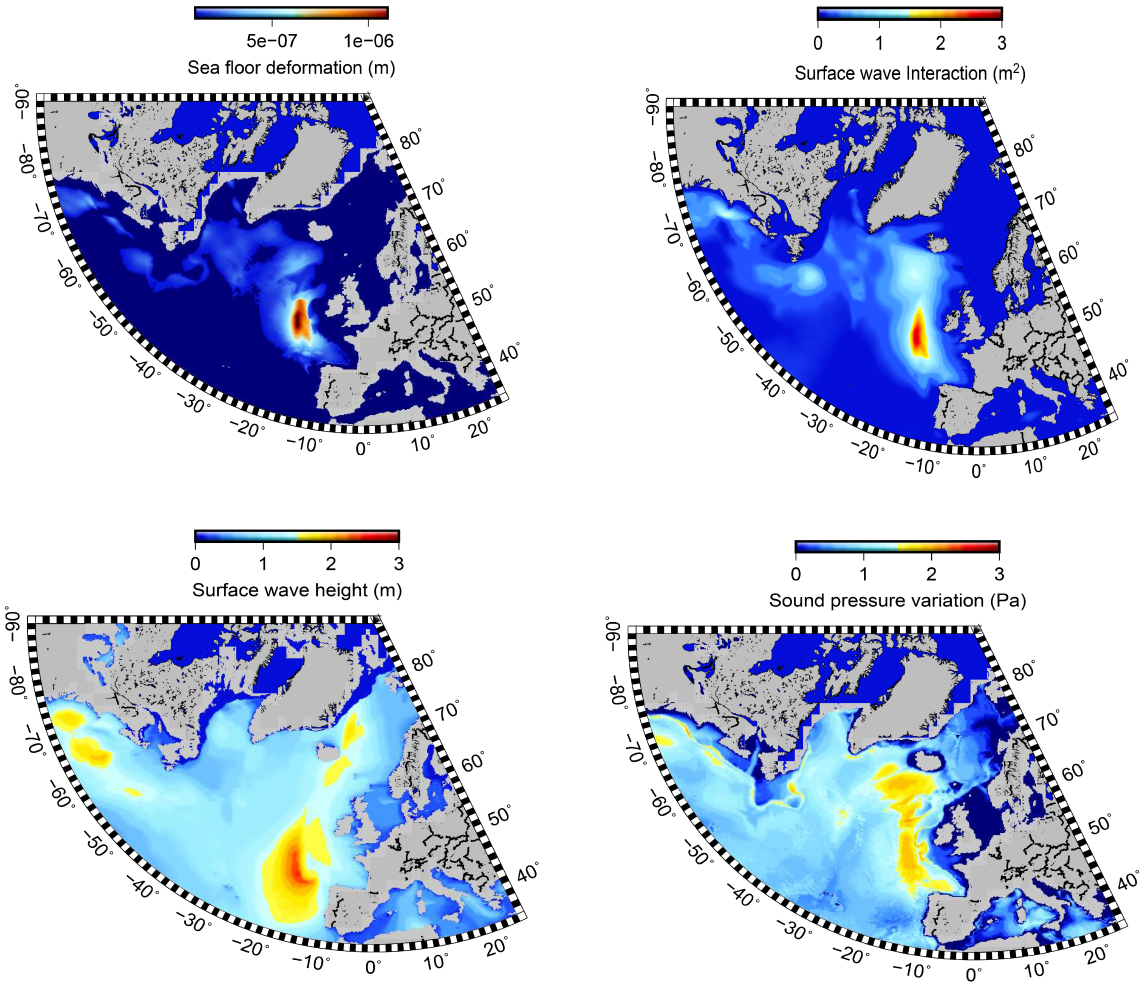

Figure 2-7: Source modeling on data of 2017-01-01T00.00.00. Left up; Sea floor displacement [Kedar et al., 2008]. Right up; Sea surface wave interaction, [Hasselmann, 1963]. Left down; Sea surface wave significant height. Right down; Bedrock pressure.

Chapter 3

Earthquake analysis

As known, the earth is not one big medium but exists out of plates. These tectonic earth plates interact with each other, Figure 3-1. In case of continental collision, Subduction and Transform faults tension between the earth plates will build up, the plates do not slide smooth side by side. At a certain point, the tension between the plates is too high and the plates pop loose. When this occurs, an earthquake occurs.

These earthquakes are regional events. Because of this, the source location is very well known. Besides, the events occur with a lot of energy. This ensures that all kind of phases are detectable at the arrays, what makes earthquakes good events to verify the ranges when each phase occurs, verify with found values in theory.

For this analysis, it is assumed that earthquakes are point sources.

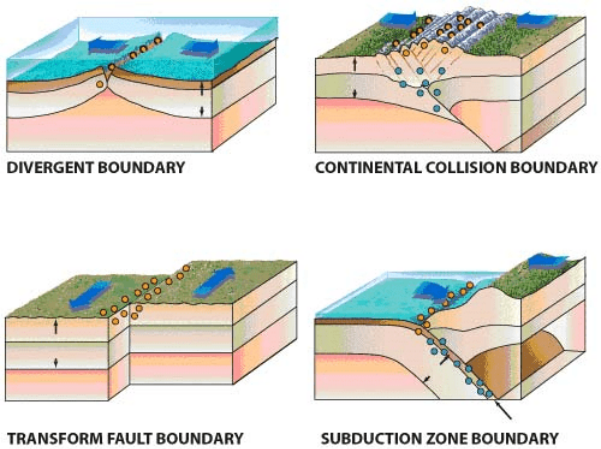

Figure 3-1: Earth plate movement what results in Earthquakes. http://www.brooklyncollegegeology.com/plates/platequiz.htm

To create a work flow and verify this work flow, five big events are used. These events are the earthquakes that happened in September and October 2011, May 2012, August and October 2016 in respectively Germany, Turkey and Italy. These earthquakes all had a magnitude around 6. See Figure 3-2 for more specific locations of the events.

These earthquakes are known events, with known source location, and recorded by many seismic arrays all over the world, Figure 3-2. The events are recorded by three component sensors, simple geophones and by CTBT arrays. Because these events had an enormous impact on civilization, a lot of knowledge is gained. This knowledge is used during this research to verify the program, work flow, and get an impression of ranges where the different phases and azimuth offsets, an issue for seismic arrays, of the signals occur.

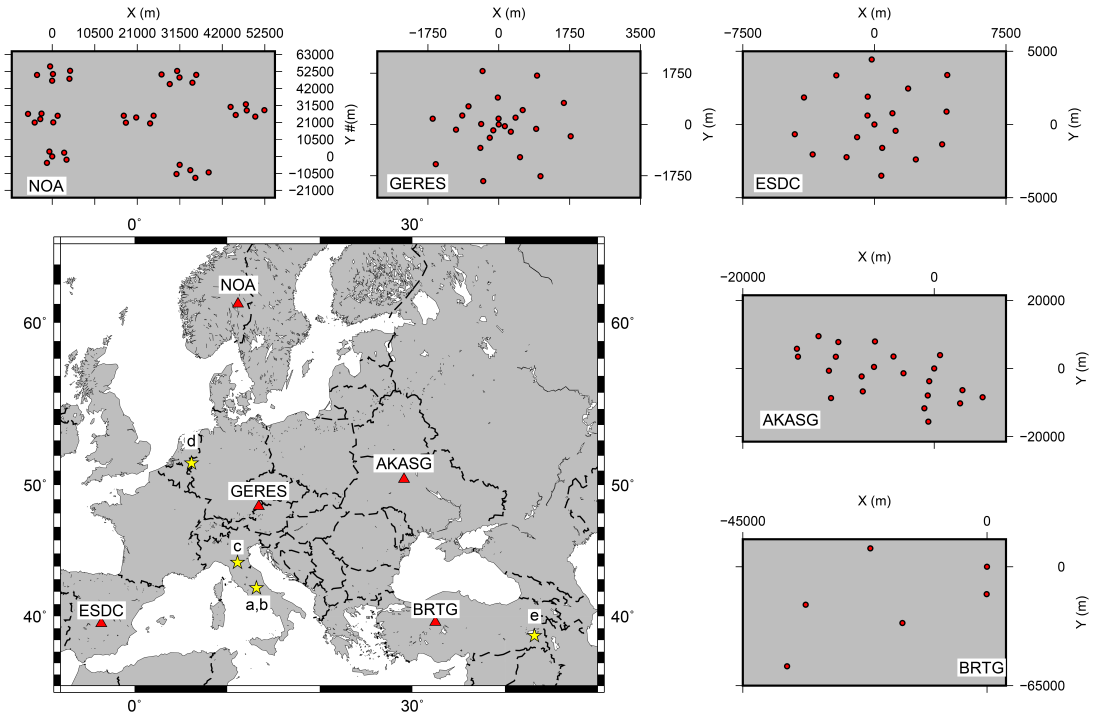

Figure 3-2: Map of Europe with used Arrays and events. Yellow stars indicate the event positions; a.) 26-10-2016 b.) 24-08-2016 c.) 20-05-2012 d.) 08-09-2011 e.) 23-10-2011. Red triangles indicate the arrays used to analyses the events.

3-1 Raw data

Loading in the data gives a good first estimation of how the data looks like, what are the amplitudes, what is the time window of interest, are there gaps in the data, can we distinguish between different phases of the signal and do all instruments give a constant response.

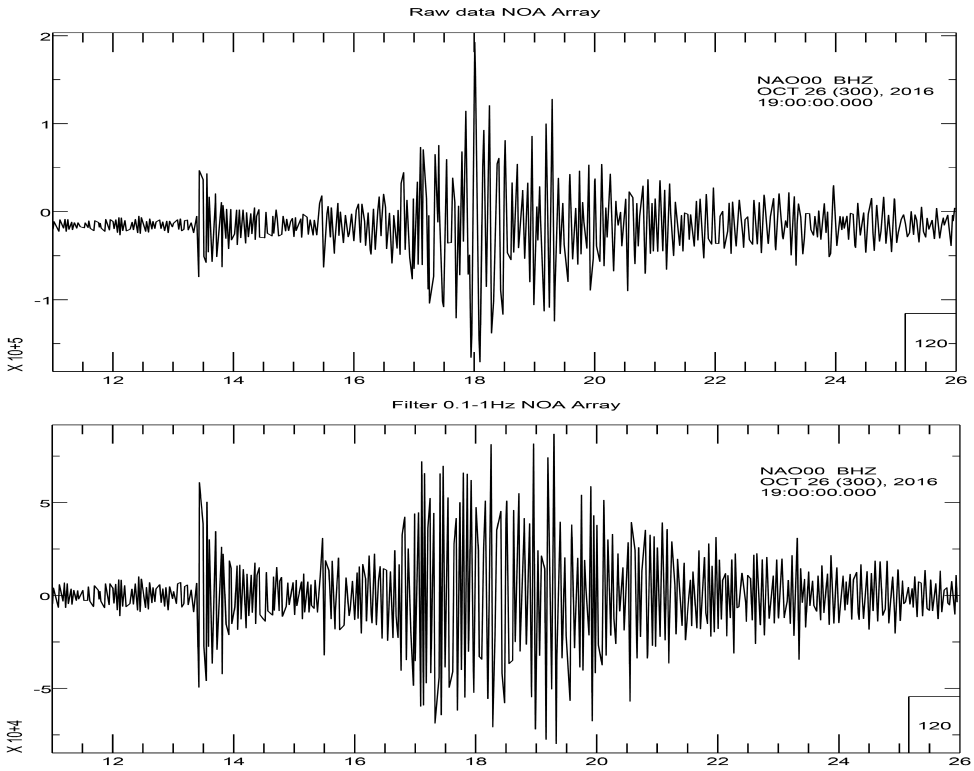

Figure 3-3: NORSAR NOA 26-10-2016 T19.00.00 Data. On top, raw data. Below, filter data between 0.1-1Hz.

To optimize the signal for processing, a Butterworth filter between 0.1 and 1 Hz is chosen, see Figure 3-3.

3-2 Beam forming

During the analysis of the earthquakes the focus is on microseisms in the phases of compressional body, shear body and surface waves. Due to the different phases, the velocity range of the signal is between 1500 m/s and 10000 m/s (with 91 steps), between these ranges beamforming is done to find the best beam. In case of good distinguishing between the surface and body waves, the data is processed twice. Once within the velocity range of the surface waves and once within the body waves velocity range.

The 'best beam' beamform method is satisfies because an earthquake is an impulsive sources. Because it is an impulsive source, it will be the event with the highest coherence, thus best beamforming satisfies.

In the Figure 3-5, one can obtain the results of the beamforming done at the NORSAR array. Out of this plots it is easy to detect the event, due to the azimuth change, SNR and the best beam. Within the interval of the event, when the amplitude increases and where several SNR peaks occur, one can observe a link between different SNR peaks and trace velocities. These different peaks with corresponding trace velocities, indicate the different phases of the signal.

The other beam forming results, of different arrays, can be found in Appendix B

3-3 Signal phases, Velocity difference

Using Figures 3-4 and 3-5, one can distinguish the different phases of the signal. To separate the different phases the signal is cut in time windows wherein one phase of the signal is detected.

By having these time windows, the data can be easily cut in a P-wave part, S-wave part and a Surface-wave part.

These different parts are analyzed individually to get more information from the data about that specific phase. For example, in which azimuth and velocity range they occur.

Figure 3-4, shows there is not much difference between the azimuth of the different phases denotable by both Figures 3-4 and 3-5. Although, there is a big difference in velocity. This indicates that velocity can be a good identifier for the different phases, as described in Chapter 2-2 but now confirmed.

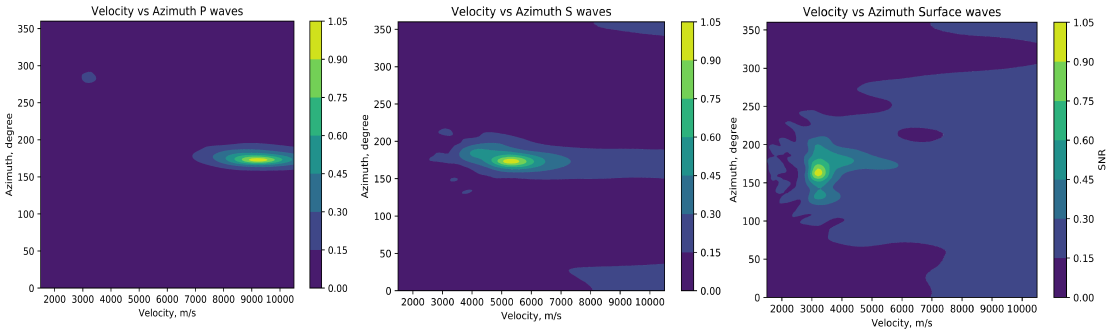

Figure 3-4: Velocity/Azimuth analysis. From left to right; P-waves, S-waves and Surface waves. Data: NORSAR NOA 26-10-2016 T19.00.00.

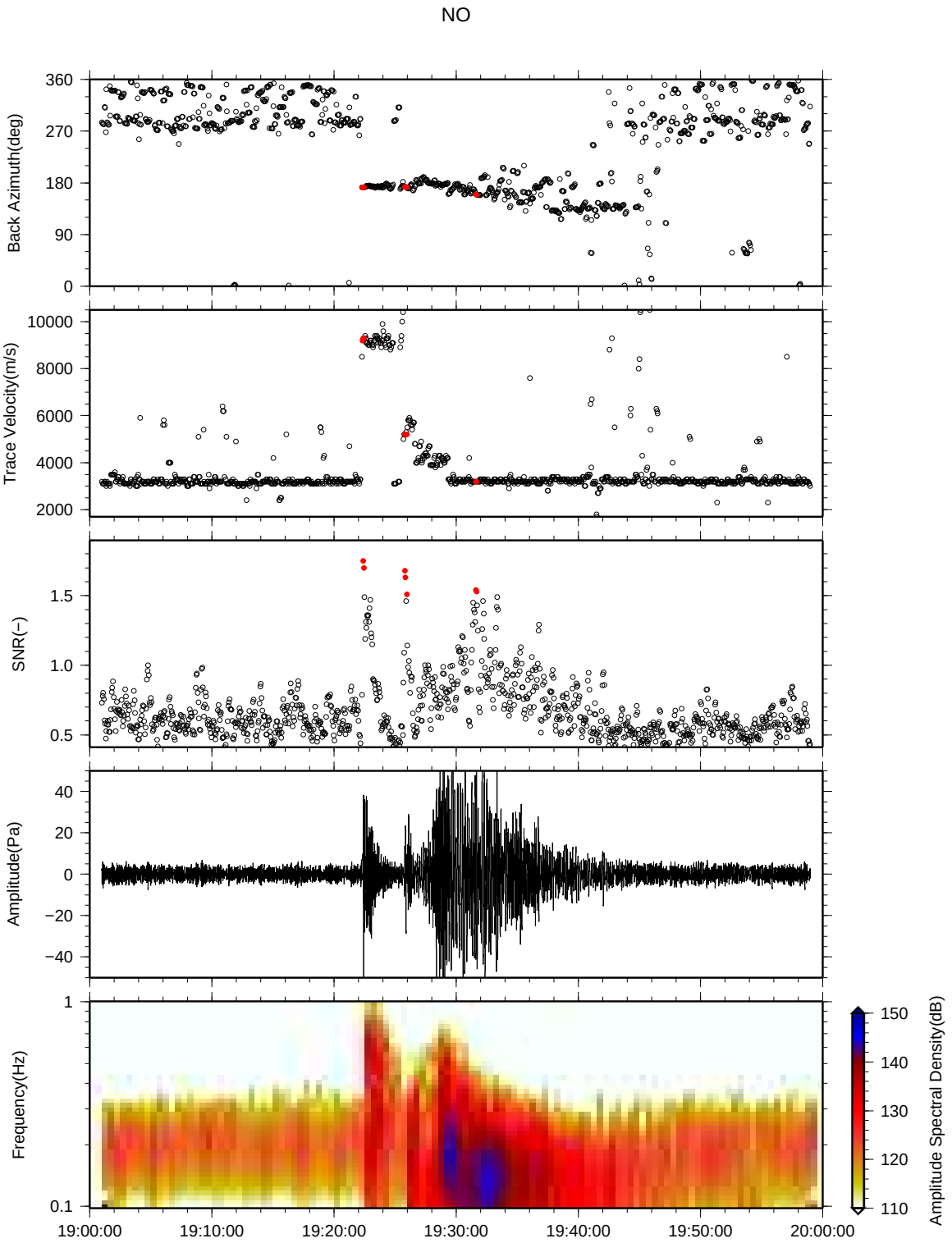

Figure 3-5: Results of Beamforming the data of NORSAR NOA array 2016 T19.00.00. From top to bottom; the measured back azimuth, trace velocity, Signal to noise ratio, the best beam and Frequency analysis. Red dotes indicate the different phases belonging to the earthquakes signal, selected on SNR value and colored in every plot.

3-4 Azimuth selection

The lobe in Figure 3-4 indicates the highest SNR values per phase. Since an accurate source location is preferable, the part with highest SNR values of the lobe is selected.

Out of the selected lobe, a range of azimuths is obtained. Chosen is to define the source location as a density ellipse. To create this ellipse, the mean azimuth and the upper and lower boundary azimuth is needed. In this research, there is chosen to use the Gaussian standard deviation to detect the upper and lower boundary back azimuth and to use the mean with its weight as upper and lower boundary.

3-5 Source location

By use of the selected azimuth range from the different arrays, a cross bearing source location can be obtained. To optimize the accuracy of the source location the phase velocity is taken constant. This is due to the lack of information considering the inclination angle of the signals over the arrays. Due to the lack of this information it is not possible to determine the true velocity out of the trace velocity.

In Figure 3-6 the source location of the 26-10-2016 earthquake becomes visible.

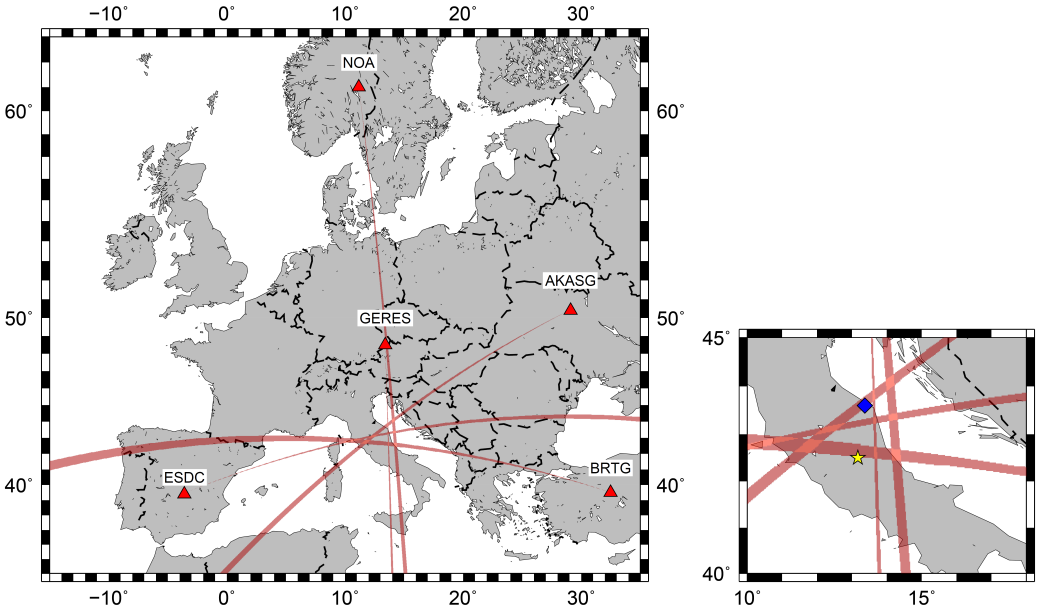

Figure 3-6: Trace back of P-wave recordings from arrays to source. Right; Zoom in on area of cross bearing, where the yellow star is the true location of the 26-10-2016 earthquake and the blue diamond the sine location calculated from the different mean azimuths.

Figure 3-6 shows that, first and most important, none of the mean azimuths is pointing to the true source location. Also, the cones do not have overlap to an area of interest, it is not possible to generate a density ellipse. This could be because an earthquake is a point source.

It was hoped that the arrays pointed more accurate towards the source. Normal earthquake analysis are done by a lot more sensors, placed over the whole world. So a small deviation is considered. Although, the source location found with arrays does have a lot bigger deviation than expected.

Chapter 4

Array Correction

Because of the obtained deviation regarding the earthquake source locations, a closer look at array sensitivity is needed. Several studies are done, considering slowness and azimuth corrections for arrays ([Berteussen, 1974], [Bokelmann, 1995], [Jacobeit et al., 2013], [Bondár et al., 1999], [Carr, 1993], [Borleanu et al., 2008], [Hao and Zheng, 2009]). All these studies consider corrections for individual arrays. [Bondár et al., 1999] created so called Slowness Azimuth static corrections, SASC, for all CTBT seismic arrays.

When applying these SASC data for the compressional body waves, there is a negative change. The cross bearing of the different azimuths does intersect further away from the true source location. When the SASC data is applied to surface waves, a slightly improved result is obtained.

Although it looks like the SASC have a positive effect on identifying the source location, there are some concerns as well. Besides a correction correction, the SASC files also provide a standard deviation for this correction factor. The correction factor, and the belonging standard deviation, differ for each azimuth. The standard deviations for the correction factor are relatively big.

This means that for each array the mean azimuth needs to be corrected with a correction factor. Besides this correction, there is also on this correction factor a standard deviation. This standard deviation comes on top of the already existing standard deviation due to processing.

When dealing with earthquakes, and so point sources, this means that the extra standard deviation is much bigger as the original standard deviation. To get a clearer image of this array deviation a side step to array sensitivity is made.

Reasons to correct

It is optimal to have an array response in the shape of a delta function, a perfect small round lobe. As shown in Appendix C, where all array responses of the used arrays can be found, it

is hard to reach the perfect lobe. Often the array has a response function wherein the lobe is more in the shape of an ellipse and tilted towards a certain direction. This results in difference in sensitivity for signals from different directions over the array. This array sensitivity causes minimal errors in the azimuth calculations, done after processing.

Besides the array sensitivity also geological sensitivity is observed by [Bondár et al., 1999], for all CTBT arrays, and [Berteussen, 1974], for the NOA array in Norway operated by NORSAR. This geological sensitivity is only applicable on body waves that enter the array from below. Surface waves experience a geological difference since they travel through the crust what makes a geological correction difficult.

Body waves travel through the Earth and will reach the array from below, with an angel of incidence. As shown in Figure 2-3, there is a big difference between the body wave velocity in the mantle compared to crust. This means that when the Moho, boundary between mantle and crust, is closer to earth surface, the waves will travel longer in this high velocity zone and so reach the array with a higher velocity. Since the sensor distance of seismic arrays is between 5 and 10 km, it is not correct to assume the geology (Moho depth) is homogeneous/constant. So, a geological correction is needed.

Creating correction factors

The best way to approach the correction for this geological sensitivity is to use the method described in [Bondár et al., 1999], [Berteussen, 1974] and [Hao and Zheng, 2009]. This method is based on correcting the observed/measured azimuths with a correction factor they obtained by theoretical back tracing of earthquakes. To get the theoretical back azimuth of this earthquake, they used velocity model IASP91 and events recorded by the National Earthquake International Center to describe the path of the seismic signals through the Earth. This results in an accurate and precise wave path with the correct back azimuth. By comparing this with the measured back azimuth, a correcting factor is found. This is done for several events (hundreds), with different directions of traveling over the array, to get for each back azimuth a correction factor.

Hoped was that the above was done for each array, while the ground underneath each array is different and so each array has different correction factors. Unfortunately, this was not the case.

[Bondár et al., 1999] provided a paper where they discussed a software, they created themselves, which makes Slowness Azimuth Static Correction, SASC, files. Theses SASC files are property of the CTBT but not complete.

NORSAR Array

NORSAR is a Norwegian research institute within the field of geoscience. Their core competencies are seismology and applied geophysics. In case of geophysics, they are involved in several monitoring operations. Think of monitoring earthquakes but also nuclear explosions. To do so, they are designated as the national data center of Norway to verify compliance with the CTBT.

Because of this, the NORSAR owns and maintains several seismic arrays in Scandinavia. Some of the seismic arrays they manage are; ARCESS, NOA, SPITS, NORES, FINES and HFS.

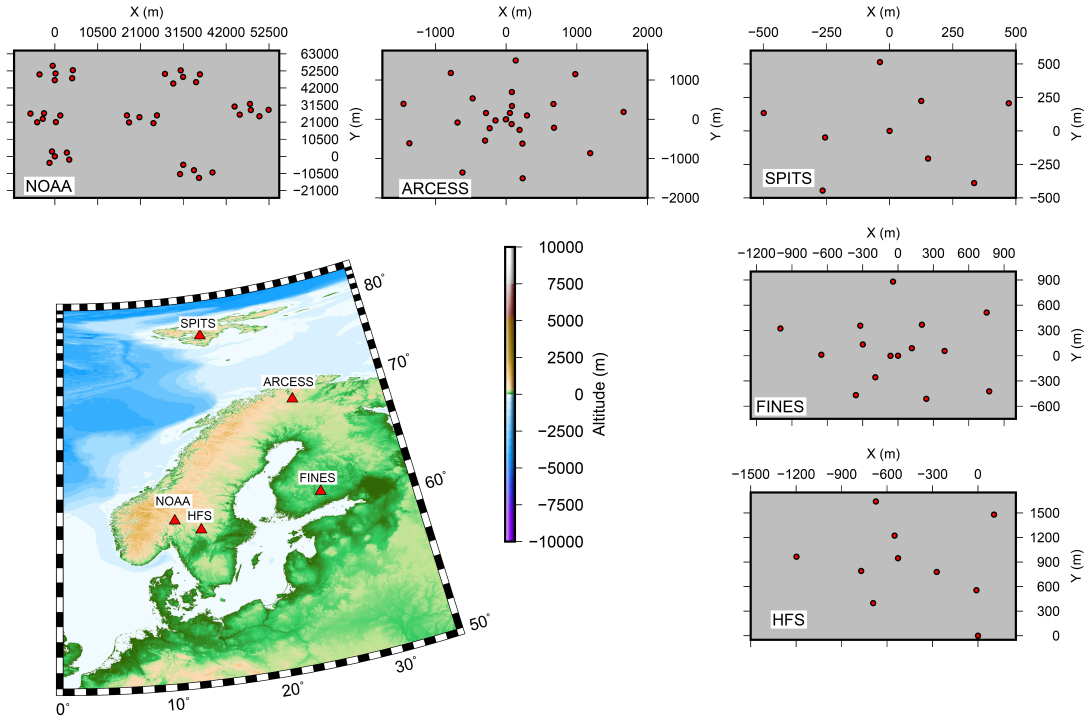

Figure 4-1: NORSAR Seismic arrays.

As described in the background information, arrays can exist of several different number and types of receivers. Table 4-1 is a summation for each of the above-mentioned arrays. Out of this one can deduct that the most promising array is the NOA array. With 42 BHZ receivers, divided in 7 sub-clusters, it is one of the biggest arrays in the world.

NORSAR Arrays				
Array	Number of receivers	Number of sub-arrays	Type of receivers	Aperture
NOA	42	7	BHZ	± 20km
ARCESS	26	4	BHZ	± 750m
SPITS	9	2	HHZ	± 200m
NORES	9	2	HHZ	± 500m
FINES	16	3	SHZ	± 300m
HFS	9	2	SHZ	± 500m

Table 4-1: NORSAR Seismic arrays

Although the NOA looks promising (personally), the observed back azimuths do not correlate with the theoretical back azimuth. Also, the trace velocity differs in value from other arrays. When comparing the trace velocity with other arrays, this is higher in case of the NOA array.

Because of this phenomenon, the NOA array is studied.

NOA array design

Mentioned before, the NOA array exists of 42 BHZ receivers placed over the south-east of Norway. These 42 receivers are divided over seven sub-clusters, what makes the NOA array a summation of seven small arrays. Because a deviation was found, in velocity and azimuth, in the previous chapter it became interesting to see why there is a difference in measured values and if there is a difference between the different sub-arrays.

Figure 4-2 shows that the full array comes close to this delta function. The sub-arrays also match with the criteria described in Evers[2008]. Although the delta functions of the sub-arrays are a bit tilted, this is not the reason of deviation.

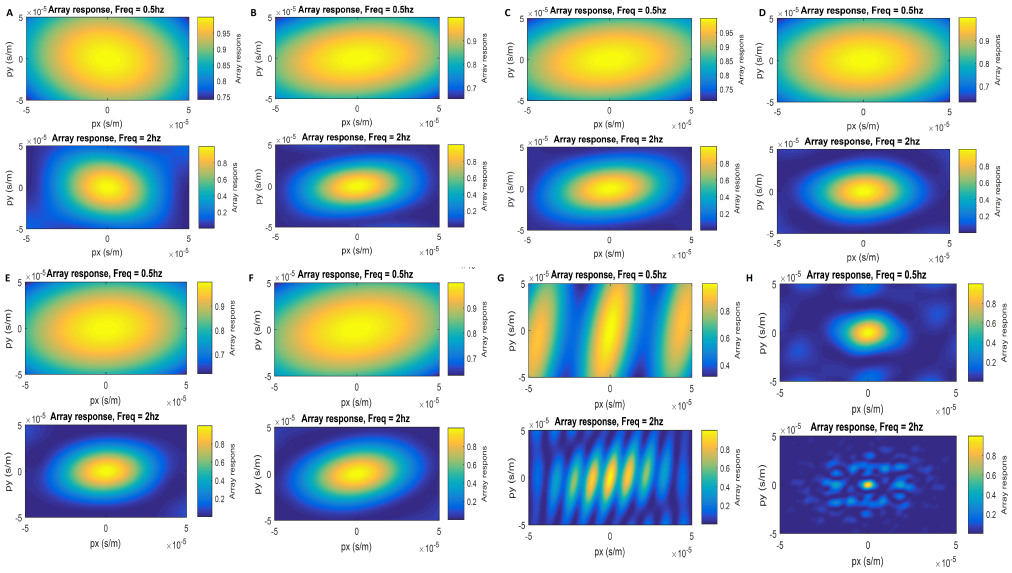

Figure 4-2: Array responses sub-arrays and full NOA array, for 0.5 and 2Hz. A.) NAO, B.) NB2, C.) NBO, D.) NC2, E.) NC3, F.) NC4, G.) NC6, H.) NOA full. Chosen to process these responses on 0.5Hz and 2Hz because the response shape is better to identify using these frequencies.

NOA analysis and Result differences

To deduct differences, or similarities, the same events as in the previous chapters are used. Instead of using the whole array to find the best beam, now per sub-array the best beam is calculated.

Comparing the trace velocities of the different sub-arrays points out large differences, see Table 4-2.

NORSAR Arrays				
Array	Trace velocity, 26-10-2016	Back azimuth, 26-10-2016	Trace velocity, 24-08-2016	Back azimuth, 24-08-2016
Theory	-	175.31	-	175.35
NOA	9150 m/s	172.80 (-2.51)	9009 m/s	174.36 (-1.01)
NAO	9140 m/s	176.63 (+1.32)	8802 m/s	176.17 (+0.82)
NB2	9075 m/s	164.70 (-10.4)	9006 m/s	175.64 (+0.29)
NBO	9399 m/s	173.58 (-2.27)	8743 m/s	177.39 (+2.04)
NC2	8846 m/s	177.54 (+2.23)	8592 m/s	175.64 (+0.29)
NC3	9196 m/s	178.41 (+3.10)	9240 m/s	177.83 (+2.48)
NC4	9550 m/s	170.87 (-4.44)	9233 m/s	171.34 (-4.01)
NC6	7946 m/s	177.29 (+1.97)	8645 m/s	176.45 (+1.10)

Table 4-2: Azimuth and Trace velocity calculated from earthquakes, 26-10-2016 and 24-08-2016 Italy, for each sub array and overall NOA array.

These differences indicate the concerns mentioned before about Moho dip. In case of the NOA array, one can assume that the wave paths from the event to the receiver, for each sub-array, is the same. Assumed the wave paths are equal for each array and considered that the array response is almost perfect for each sub-array, the difference in trace velocity can be linked to the Moho dip. In [Berteussen, 1974] this Moho dip was first described for the NOA array in context of azimuth and slowness correction, later also in [Bondár et al., 1999].

Although a slowness correction has been calculated for the NOA array by [Berteussen, 1974], one can deduct out of [Berteussen, 1974] that there is a zero slowness correction factor for events coming from the south (back azimuth around 180◦), like our events. This indicates that the difference in trace velocity can be completely transferred to the difference in geology beneath the sub-arrays.

Besides differences in trace velocity, also differences in back azimuth is found. In Table 4-2 the obtained back azimuths, per sub-array and overall array, are listed. [Berteussen, 1974] and [Bondár et al., 1999] made azimuth corrections for the NOA array. When comparing these two correction models, Berteussen tells to correct by 4 degrees, figure 3.3 [Berteussen, 1974], while Bondan does not correct.

NOA geology

There are some large differences between the NOA sub-arrays. Unfortunately, the correction files of Berteussen and Bodan do not contribute to an improvement of the results. This indicates that the difference is most likely due to crust thickness, Moho depth.

[Ottemöller and Midzi, 2003] discussed the crustal structure of Norway. In their research they validated the Moho calculations of [Kinck et al., 1993], by inversion of teleseismic receiver functions. [Ottemöller and Midzi, 2003] updated the Moho depth beneath the Norwegian arrays and showed a more detailed depth profile. In case of the NOA array this resulted in a Moho depth between 32 and 34 km.

Having a closer look at the Moho depth underneath the NOA array, Figure 4-3, shows that there is indeed a variation in Moho depth.

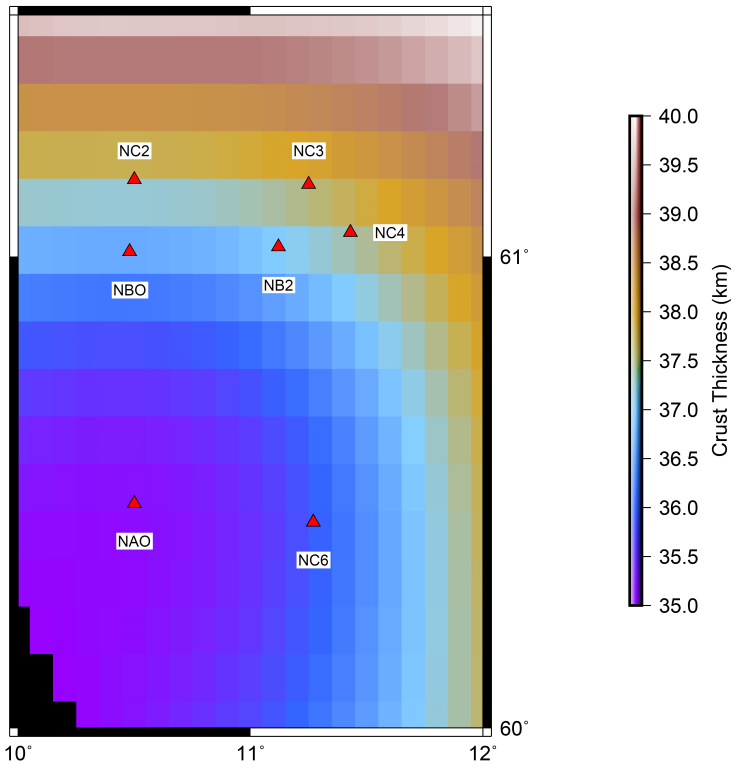

Figure 4-3: Moho depth underneath the NOA array, GMT plot of the European Moho depth profile. [Moh,]

The results of [Ottemöller and Midzi, 2003], and Figure 4-3, confirms that the Moho is not at a constant depth underneath the NOA array, the Moho dips. Although, there is not a correlation between Moho depth and the differences in trace velocity.

When the Moho is close to the earths surface a higher trace velocity is expected in comparison with a deep Moho. The explanation is that the compressional body waves do not come from nadir they are arriving under an inclination angle. Due to this inclination angle it is even harder to obtain a correlation between the Moho dip and the trace velocities. This is the reason for deviation of velocity and azimuth between the different sub-arrays.

Chapter 5

Deep ocean microseisms observations

Continuous microseisms are called ambient noises. Sources for these kind of microseisms are for example ocean wave interaction, storms or calving glaciers.

[Gerstoft and Bromirski, 2016] showed that so called Weather bombs induce seismic signals. A Weather bomb is an intense weather system such as a storm, like a cyclone. A fraction of the energy, generated by ocean wave-wave interaction at the ocean surface, resonance towards the sea floor and couples into seismic surface and body waves, microseisms (see Figure 2-6).

[Gerstoft and Bromirski, 2016] showed the propagation of a storm in the North Pacific ocean, detected by the Southern Californian Seismic Network, Figure 5-1. This indicates that storms can be identified by seismic arrays and thus storms can be used to deduct more information about the coupling factor between ocean and sea floor.

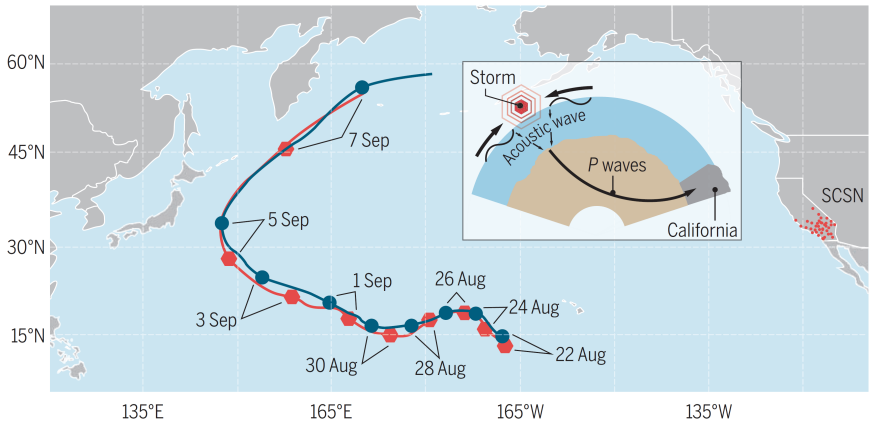

Figure 5-1: Movement of a storm over the Pacific Ocean causing microseisms. [Gerstoft and Bromirski, 2016]

5-1 Arrays and Data

To study ambient noise CTBT arrays in Europe are used. From 01-01-2017 till 01-03-2017 the seismic recordings of AKASG (Ukraine), ESDC (Spain), GERESS (Germany), NOA (Norway), ARCESS (Norway) and SPITS (Norway) are processed and used to detect ambient noise and localize by use of beam forming.

To choose a region of interest, with respect to ocean wave-wave interaction, the ECWF WAM model is used. The Atlantic ocean, specific region around and above Iceland, shows a lot of activity.

Since the ocean wave-wave interactions, due to storms and/or swells, are of interest. It is necessary to know other deep ocean, or near coastal, microseismic sources. It is essential that all earthquakes, occurred in the chosen time window, are known (see Table 5-1). The founded earthquakes did not happen in the region of interest. Assuming only direct arrivals of these earthquakes are visible in the recordings, these earthquakes will not influence the processing and detection/localization of ambient noise. This because when using cross bearing the arrays will not overlap in the region of interest, what makes them side information.

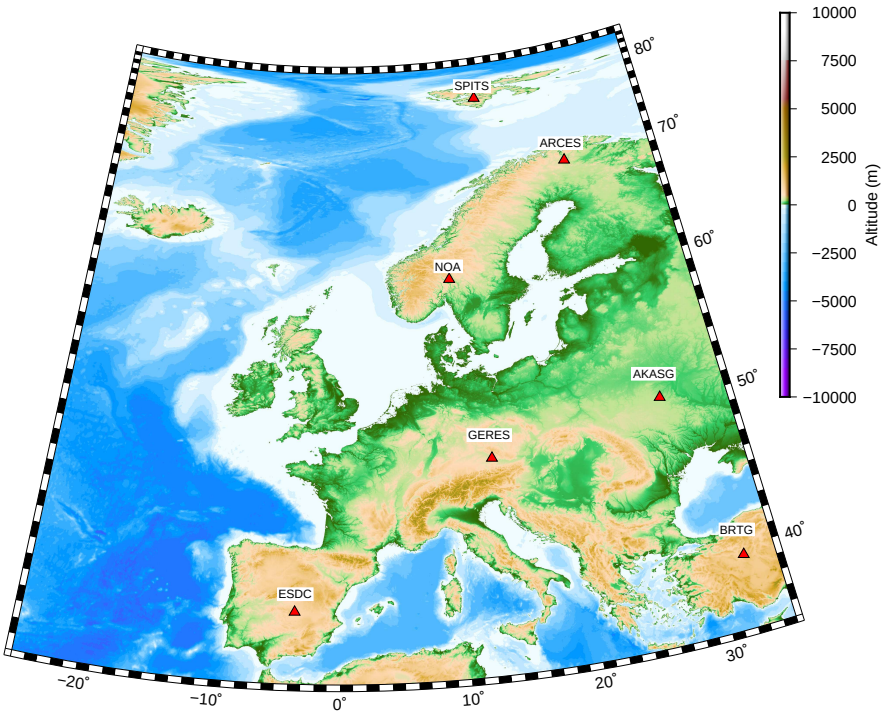

Figure 5-2: CTBT Arrays used to detect and localize ambient noise.

Earthquakes		
Date	Location	Magnitude
02-01-2017	Fiji Islands	6.3
03-01-2017	Fiji Islands	7.0
03-01-2017	Fiji Islands	6.0
08-01-2017	Devon Islands	6.1
10-01-2017	Celebes Sea	7.3
10-01-2017	Solomon Islands	6.4
14-01-2017	Fiji Islands	6.0
19-01-2017	Solomon Islands	6.7
22-01-2017	Bougainville	7.9
30-01-2017	Vanuatu	6.0
07-02-2017	Pakistan	6.2
10-02-2017	Philippines	6.5
18-02-2017	Argentina	6.4
21-02-2017	Bolivia	6.5
24-02-2017	Fiji Islands	6.9

Table 5-1: Recorded earthquakes between 01-01-2017 and 01-03-2017 with magnitude six or higher.

5-2 Processing

Numerical modeling

By use of the WAM and the theories of [Hasselmann, 1963], [Kedar et al., 2008], [Obrebski et al., 2013], [Ardhuin and Stutzmann, 2010] and [Smets,] several different models are created to indicate the microseismic source areas.

After analysis of the 2D wave spectra obtained from a coupled ocean-atmosphere model, ECMWF WAM, assimilating buoy and satellite data. Globally analysis fields with 14km horizontal resolution and 6hr intervals. Wave spectra consist of 36 frequencies (0.0345-0.9695 Hz) and 36 directions.

This research will use the sea floor displacement, [Kedar et al., 2008], and the ocean wave-wave interaction, [Hasselmann, 1963] to characterize the source area. The 2D wave spectra, from ECWMF WAM, are used from January and February 2017 with 12 hour intervals.

CTBT Data

To process the observed array data, beam forming is used. For each array the 'best beam' is calculated for each part of the signal, bins. Before splitting the recordings, the data has been filtered with a bandpass filter between 0.1 and 1 Hz. To obtain this best beam, a bin size of 51.2 seconds is taken with an overlap of 50%. Over these bins, beam forming is done in velocity ranges from 1500 m/s till 10500 m/s (91 steps) and in back azimuth ranges from 0° till 360° (720 steps).

Because the WAM data is stacked every 12 hours, the CTBT data also needs to be stacked. During post-processing the CTBT data is stacked within bins of 12 hours. Over these bins, the average back azimuth is obtained with its standard deviation.

The source area is moving during these 12 hours. The mean back azimuth will give a indication of the source location, with the standard deviation as error bar. When the amount of standard deviation is over 25° this indicates that there are two main events recorded. In this case, more detailed processing is needed, with focus on both events.

5-3 Interpretation

To get an idea about the source location by use of the CTBT data so called cross bearing is used, see section 2-5. By use of the mean azimuth and standard deviation, cones can be drawn back from receiving array to source location. The intersecting area is used to indicate the source area, which is compared with the simulated source area.

SNR range and phase difference

A high SNR indicates a signal, coherence between microseisms. In case of ambient noise, the high SNR values are used to detect the source locations. Very high SNR events are suspicious, thus needs to be removed.

The high SNR events often come from local events. Think of local earthquakes or an array that is orientated near the coast and thus record the ocean wave interaction with the coast.

As said, also the array location, geology beneath and local features around an array influences the spectrum of SNR values. This means that every array has a different range of SNR values wherein ambient noises can occur.

The SNR range of an array can be indicated by use of a Box plot like Figure 5-3. In such a box plot it is easy to indicate the distribution of data points over velocity and SNR. Out of this box plot, created after best beam forming, it becomes clear if an array records dominantly Surface waves or Body waves as best beam. Also the range of SNR wherein these phases occur are interesting.

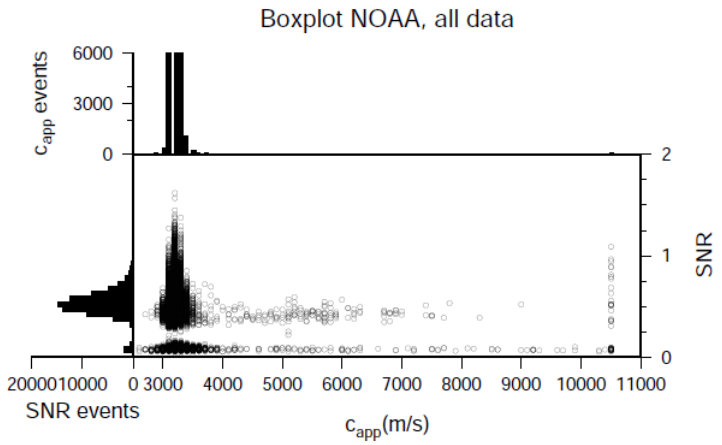

Figure 5-3: Boxplot of the NOA array after 'best beam' processing, data from 01-01-2017 till 01-03-2017.

In case of this research, searching for the origin of ambient noise and to locate, both phases of the signals are interesting. Surface waves will indicate local events where body waves indicates events that occur further away of an array.

So this means a more detailed look will be held on all phases within the SNR range indicated in Table 5-2.

Stacking

Since the simulated microseismic sources are available every 12 hours (due to computational reasons, WAM files cost a lot of memory), it is needed to stack the observed data. To do so, 12 hour bins are created around the WAM analysis time, 6 hours before and after.

Noise is not an impulse source, so the impulsive sources needs to be filtered out. Impulsive sources have a high SNR and occur rarely. A first step of filtering is to define a range of SNR values of interest, Table 5-2. This SNR range filters most of the impulsive events. To be sure all are filtered out, a minimum of 60 events per 12 hours is required. Impulsive events do not occur continuously, so to filter these impulsive events out a specific SNR range and minimum limit of events is used. After filtering out the impulsive events, the mean - standard deviation and weight of the mean is calculated over the stacked observed data.

By use of the mean, standard deviation and weighted mean, two different types of interpretation can be done. So called Gauss interpretation, where the mean azimuth and its Gaussian standard deviation is used per array to create the cones. Or a circular deviation. This deviation creates cones based on the mean azimuth and its weight, the bigger the cone the less weighted the mean while having a small cone means that the mean is high weighted.

SNR selection arrays	
Array	SNR range
NOA	0.5 - 1
ARCESS	1 - 4
SPITS	1 - 4
AKASG	1 - 2
ESDC	1 - 3
GERESS	1 - 2

Table 5-2: SNR ratios per array, determined by analyzing the box plots, Appendix A

5-4 Analysis

5-4-1 Individual array analysis, Best Beam method

Before an overall analysis will be done, comparing the simulated and observed data, it is useful to do an individual analysis. Are the recordings coming from sources in the Atlantic ocean or do they come from local sources, and what kind of signals does the array record?

NOA

Having a look at the box plot of the data from NOA, Appendix A-1, and at the beamforming analysis, Appendix B-1, shows that the NOA array mostly shows surface waves after best beam forming. The Signal to Noise ratio has a value between 0.5 and 1 what indicates that the recordings are noises. The frequency of most the recordings is between 0.1 and 0.3 Hz what indicates microseisms.

Combining this with the knowledge obtained from [Bromirski et al., 2013] and [Yang and Ritzwoller, 2008], who showed in there research that only a little fraction of surface wave microseisms, generated in the deep ocean, are recorded by continental seismic array, confirms our results. Since the NOA array is located in the south of Norway, surrounded by fjords, our observations strongly links to [Bromirski et al., 2013] and [Yang and Ritzwoller, 2008] conclusions, that the recorded surface wave microseisms are due to near coastal wave activity.

ARCESS

When analyzing the ARCESS data, with the knowledge of the box plots (Appendix A-2) and the best beamforming results (Appendix B-1), one can conclude that the ARCESS array records mostly non microseismic signals. The recorded frequencies are higher than what to expect.

From the boxplots it is easy to conclude that the ARCESS array shows more surface waves than body waves after best beamforming. This, and the high SNR indicates that also this array records strong local events. Having the knowledge of [Bromirski et al., 2013] and [Yang and Ritzwoller, 2008] plus the localization of the array, surrounded by fjords and near a ocean-continental ridge, indicates that the array is dominated by near-coastal noises.

Besides the surface wave recordings, the array also detected shows some body waves. After analyzing the possible local sources and been in contact with the researchers of the project CalvingSEIS, Univ. of Oslo, it became clear those body waves could be generated from the local earthquakes near Svalbard, Spitsbergen. [NORSAR-January-Database, 2017] and [NORSAR-February-Database, 2017].

SPITS

The SPITS array shows a similar behavior as the ARCESS array. Out of the boxplots, Appendix A-3, and the beamforming process, Appendix B-2, it becomes clear that the SPITS array mostly records events with higher frequencies as microseisms. Also the SNR ratios of this array are high what indicates strong local events. Main difference with the ARCESS array is that the SPITS array records more body waves as the ARCESS array does. This could be due to the local earthquakes near Svalbard, [NORSAR-January-Database, 2017] and [NORSAR-February-Database, 2017].

Other possible sources could be glacier activities and near coastal activities. Glacier activities are impulsive signals, non continuous, around 1 Hz. The combination of 'high' frequencies and high SNR values recorded by the SPITS array could indicate glacier activity. Although, the recordings and the processing results, Appendix B-2, do show low frequencies. Since the array is placed on Spitsbergen, surrounded by ocean, it could be suggested that the microseisms come from near coastal activities.

AKASG

Having a look at the information of the AKASG array, boxplots (Appendix A-4) and best beamforming (Appendix B-2), shows that this array shows almost only surface wave microseims. The SNR values are between 1 and 2.

Something noteworthy is that all the recordings have the same back azimuth. The array points constantly towards the Baltic sea. This could indicate that the array is constantly recording actions from the Baltic sea. [Nikulins, 2017] shows that some seismic noise sources in the Baltic Sea. Although, the frequencies of these sources are to high (out of the microseisms range). After personal communication with Mr Nikulins, it became clear that the Baltic region deals with 'mini-tectonic' sources. Besides the nature tectonics, other sources for microseims could be the exploration of fossil fuels in the Baltic Sea. Mr Nikulins told me there is exploration and extraction of Shale gas going on in this region, a possible source.

To be sure these recordings are generated in the Baltic sea region, a second array is preferable to confirm. Unfortunately there is not a second array to confirm this thoughts and thus the Baltic sea as source regions stays a guess.

ESDC

After analyzing the ESDC array, boxplots (Appendix A-5) and best beamforming results (Appendix B-3), it becomes clear that the array mostly records surface waves with SNR between 1 and 3. The recorded frequencies are between 0.1 and 0.3 Hz what indicates microseisms.

The array suggest that the recordings are coming in from the west. At the west side of the array is the continental steep ridge of Eurasia, Portuguese coast. It looks like most of the recordings are generated at this ocean-continental ridge, with would confirm [Bromirski et al., 2013] and [Yang and Ritzwoller, 2008] thoughts.

GERESS

The GERESS array shows after analyzing, boxplots (Appendix A-6) and best beamforming results (Appendix B-3), an even distribution of recorded surface waves and body waves. Also the SNR values are not to high, what indicates more ambient noise like behavior. Having a closer look at the frequencies of the recordings shows that most of the recordings are to high for microseisms, around 0.5Hz, what could indicate non microseisms or higher order microseisms, non primary microseisms what is not the main focus of this research.

The above makes the GERESS array one of the most promising arrays with respect to recorded body waves. The positioning of the array, at the border of Czech - Germany - Austria, indicates non near coastal microseisms as dominant source. Also the distribution of the different phases look promising.

GERESS array is operated by BGR, German Federal Institute for Geosciences and Natural Resources, and mainly used as a single detector. Localization processes is not often done by using the GERESS array. Hence, no information about localization accuracy as well about the SASC files.

5-4-2 Individual array analysis, Clean method

Besides the 'best beam' beamforming, also the 'clean' beamforming is applied to a part of this data set. Out of the numerical simulation it became clear that there was a lot of ocean wave interaction on 10-02-2017.

For all arrays, the data set has been focused on 0.2Hz and split into 86 bins, where each bin itself has been split into 40 sub-bins. First a total power spectrum has been calculated for these bins by following the Bartlett beamforming.

When completed, for each bin a cleaned power spectrum has been calculated iteratively. Done with 150 iterations and a control removing parameter, ϕ see section 2-4, of 0.1.

Analyzing the results of these power spectra shows that for the ARCESS and SPITS arrays a more detailed analysis needs to be done regarding the parameters for the cleaning process, both show one maximum (no improvement in comparison with the best beam method).

AKASG

The other arrays do show an improvement. The AKASG array did show only recorded surface waves after the best beam method. After cleaning the spectrum it became clear that besides these surface waves also body waves are detected.

Out of Figure 5-5, top, it becomes clear that the previous conclusion, about the noises from the Baltic Sea, were correct. Although, the best beam method only showed detected surface wave while the clean method shows there are also body waves detected from the same region. Besides the correlation between surface waves and body waves found from the Baltic Sea region, the cleaned power spectrum does also shows body waves arriving with a back azimuth that can be linked to the ocean wave-wave interaction on 10-02-2017.

NOA

The NOA array also shows a interesting result after the clean beamforming. The conclusion of only recorded surface waves, made after the best beam analysis, is correct. But it becomes clear that there is not just one source for these surface waves but several.

Figure 5-5, second from above, shows there are two main sources for surface waves. These two sources can be linked to near coastal activities. Unfortunate, the NOA array does not record body waves generated from the wave-wave interaction.

GERESS

The best beam method showed for the GERESS array an even distribution for detected body and surface waves. Out of the clean method it becomes clear that the GERESS array does detect the body waves, generated from the wave-wave interaction, very well. Besides it also records surface waves directly from the south, indicating the Mediterranean sea, Figure 5-5 (second from below).

ESDC

The same kind of conclusions (for GERESS) were made for ESDC after the best beam method. Only detected surface waves. After cleaning the power spectrum of the ESDC array a lot of 'side' maximum appear. The thoughts about near coastal dominated surface waves is confirmed. Out of Figure 5-5, bottom, it becomes clear that the ESDC array records a lot of surface waves generated from the west, Portuguese coast, as from the east, Mediterranean sea.

The ESDC array does show a maximum coherence within the back azimuth range, regarding the wave-wave interaction and the ESDC array. But most interesting, besides the maximum (surface wave) it also shows a detection in same direction for body waves.

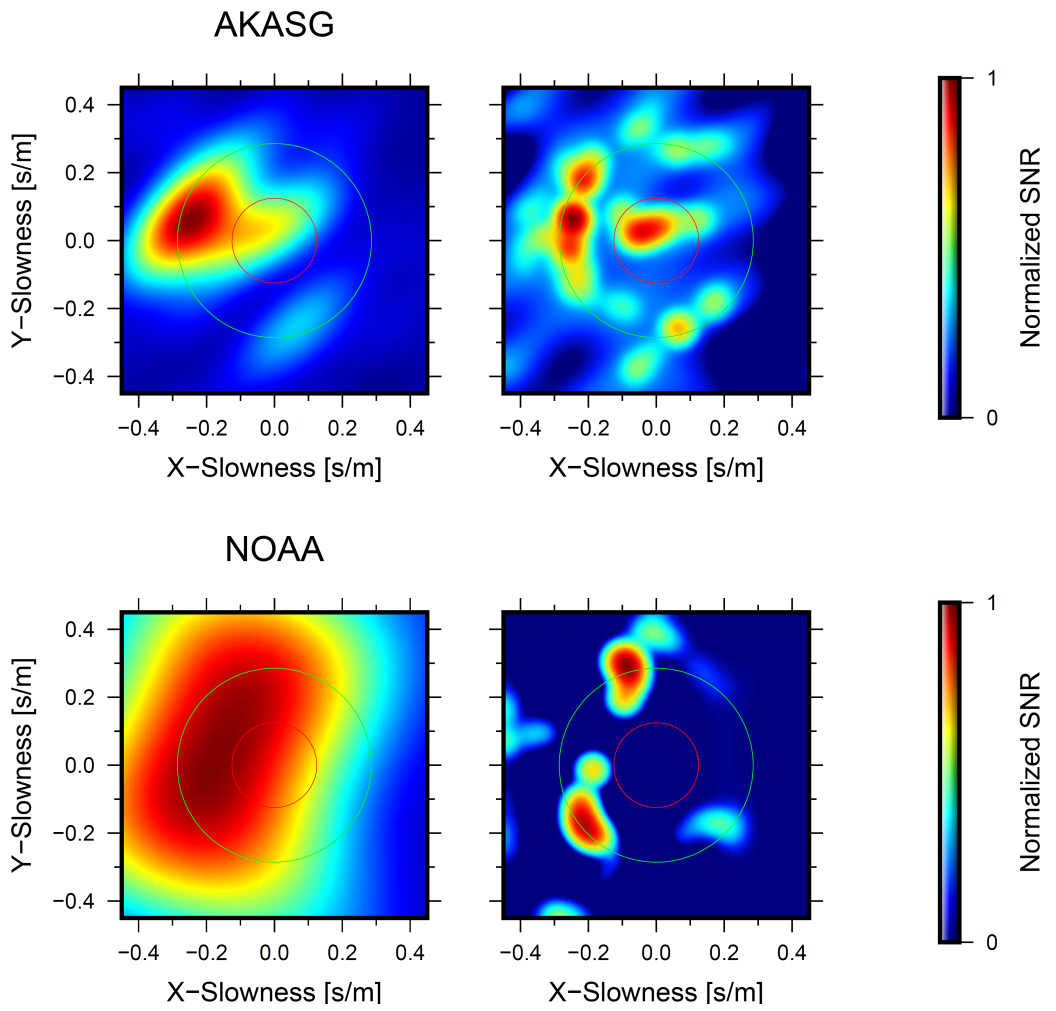

Figure 5-4: Clean power spectra for the arrays from top to bottom: AKASG and NOA on 10-02-2017.

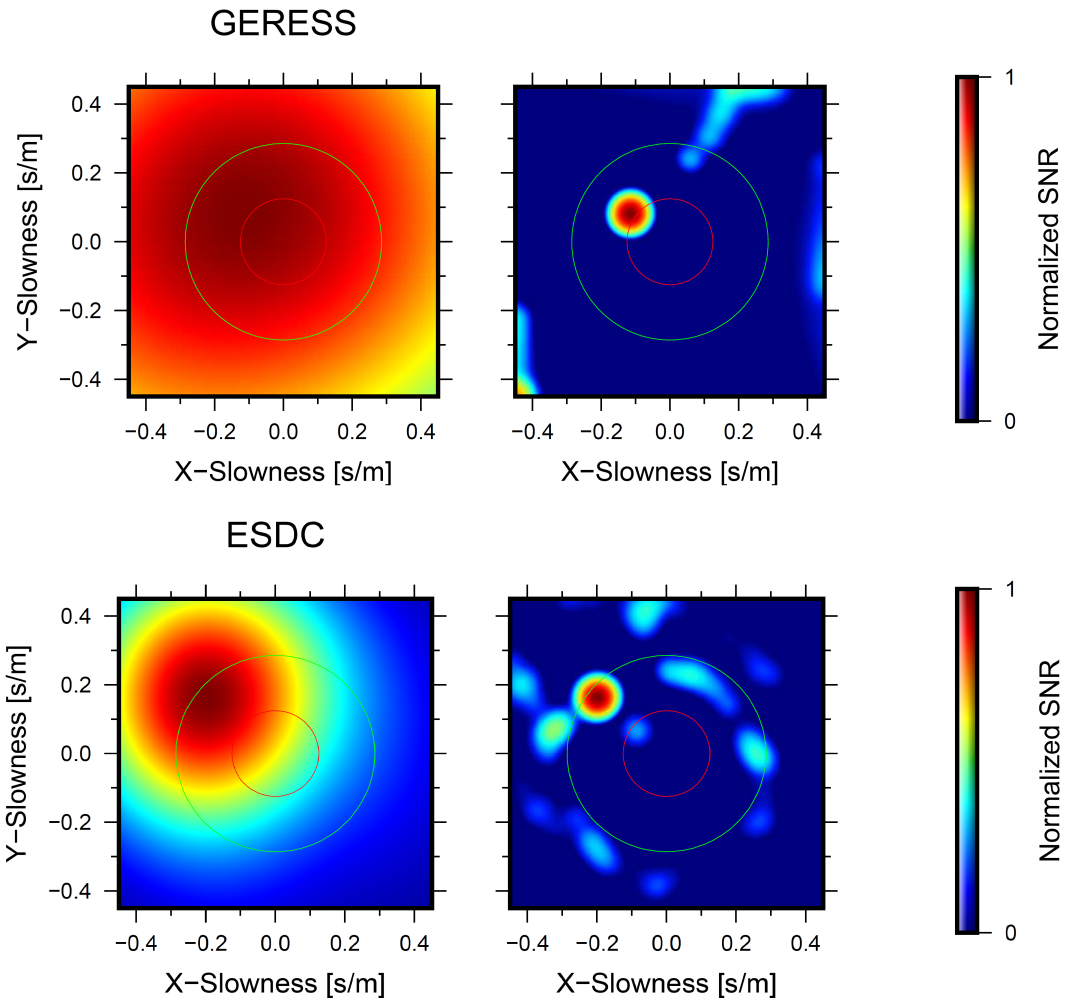

Figure 5-5: Clean power spectra for the arrays from top to bottom: GERESS and ESDC on 10-02-2017.

5-4-3 Overall analysis

By use of the WAM models, four periods of high ocean wave activities are selected. Suggested is that during these periods strong microseisms are generated. The periods are listed in Table 5-3. By use of cross bearing the calculated 'trace back cones', a comparison between the observed array data and the numerical approach from WAM, can be made.

Dates for comparison array and WAM data	
	Time span
1	01-01-2017 till 04-01-2017
2	11-01-2017 till 14-01-2017
3	28-01-2017 till 01-02-2017
4	09-02-2017 till 15-02-2017

Table 5-3: Dates with large ocean wave-wave interaction, analyzed by use of the WAM model.

After analyzing all the arrays, with the 'best beam' and 'clean' method, it becomes clear that the body waves are the most interesting phase regarding to the ocean wave-wave interaction. This due to the near-coastal interactions that generate surface waves, that overwhelm surface waves generated by the wave-wave interaction.

When comparing the results of the best beam beamforming and the clean beamforming, it is clear that the clean beamforming is more promising due to the detected body waves. This is confirmed in Figure 5-6. The trace back cones are drawn after best beam analysis. Since only the best beam is saved by the best beam method a lot of information is thrown away.

The results of the clean beamforming in Figure 5-7 shows an interesting overlap of the trace back cones, of AKASG - GERESS - ESDC arrays. When validating this with the simulated data, it shows an overlap near the numerical calculated source area. Although, this is a rough approach of the clean analysis. The mean azimuth and its standard deviation needs to be calculated with higher accuracy. In this example a standard deviation of 15$\circ$ is chosen to create the cones.

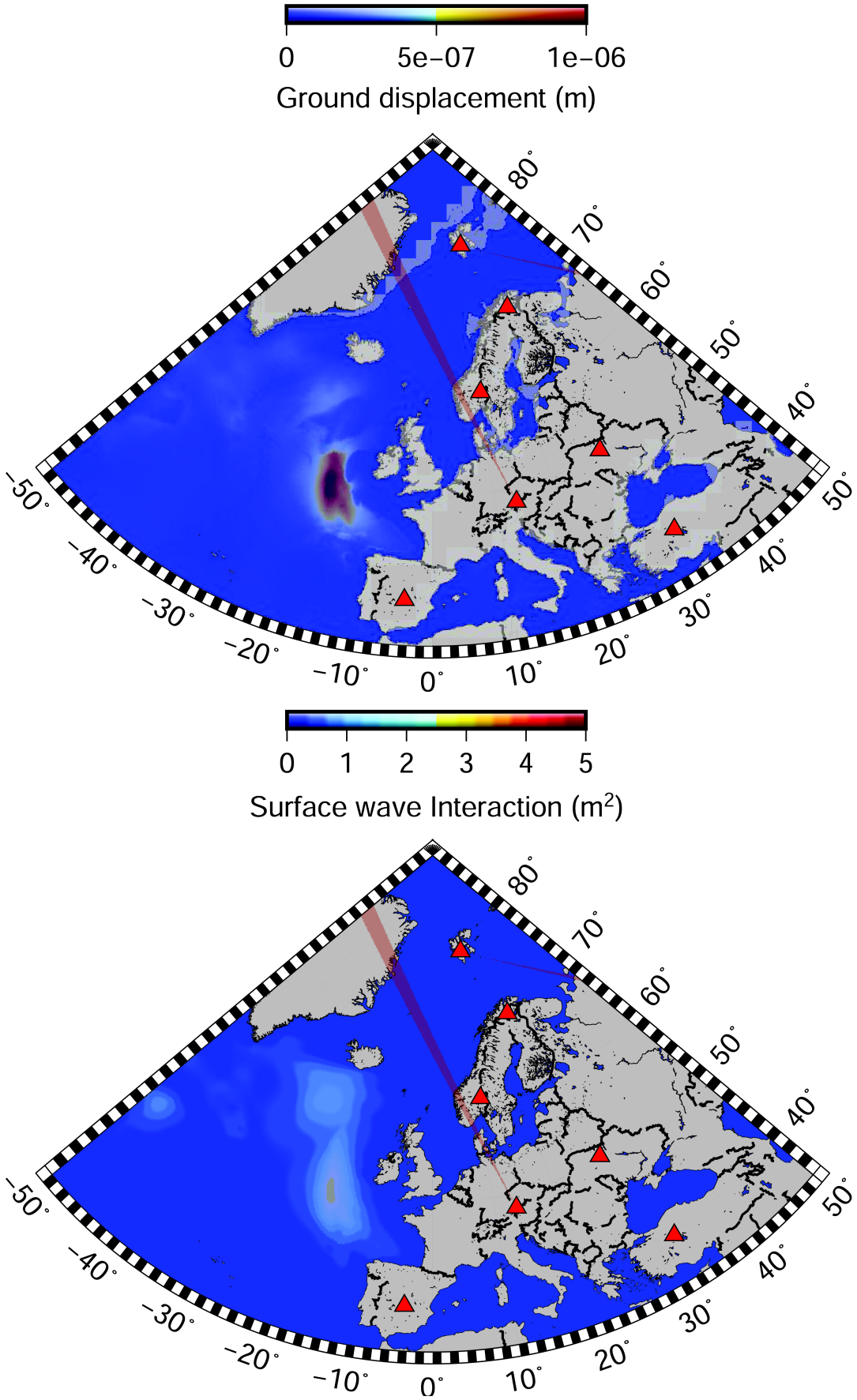

Figure 5-6: Comparison between observed best beamforming data and numerical simulated data, body waves on 10-02-2017.

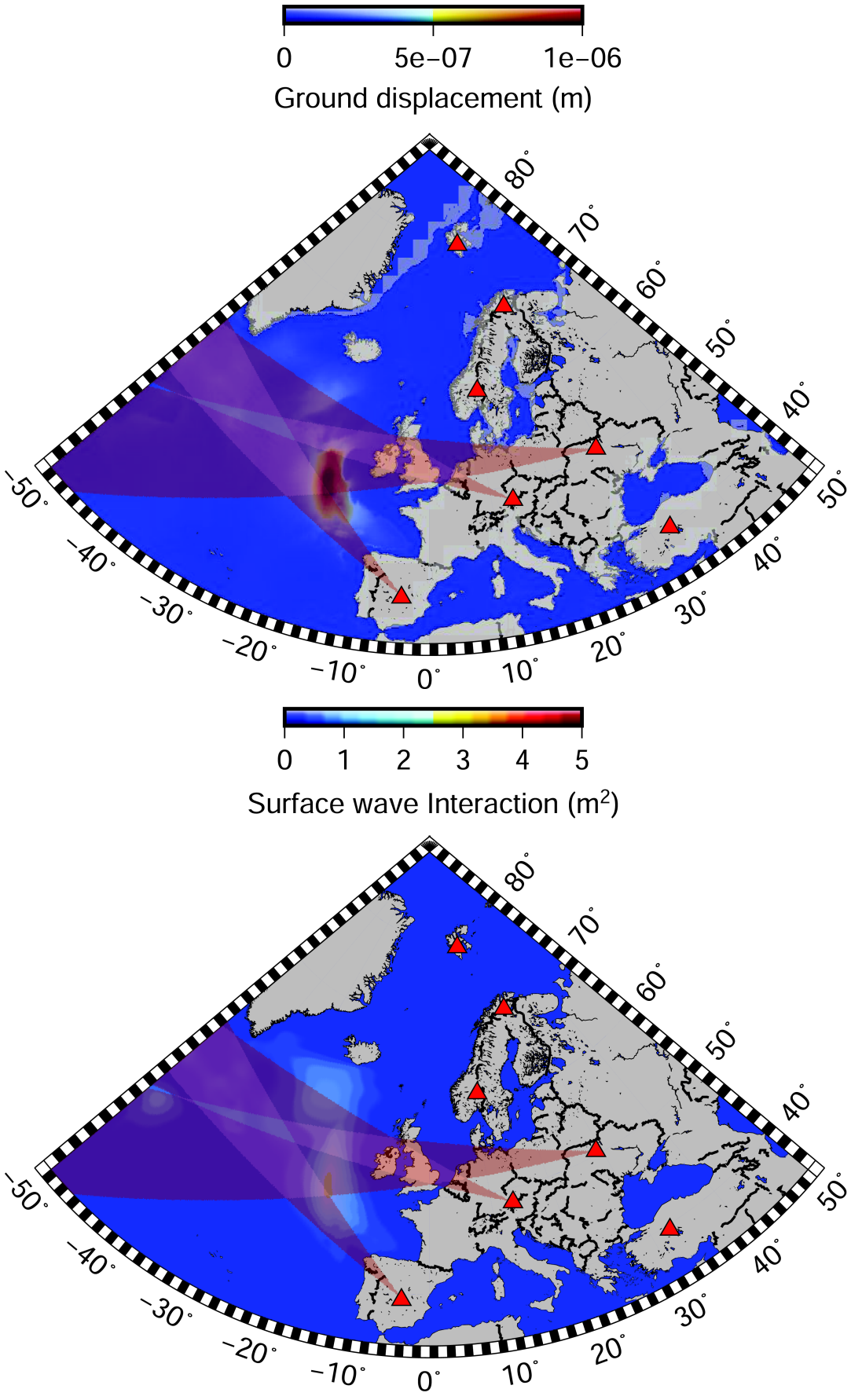

Figure 5-7: Comparison between observed cleaned beamforming data and numerical simulated data, body waves on 10-02-2017.

Chapter 6

Conclusion and discussions

Array correction

In order to have the highest accuracy in localization of an event, it is necessary to have full knowledge of an array. Think of direction sensitivity (shape of response function), geological sensitivity (Moho depth) and inter-receiver spacing plus altitude difference.

During this research so called 'trace back cones' are used. These cones indicate the area a recorded event possibly comes from, drawn from the array towards source location. One can imagine, the less accurate the recording - the bigger the cone will be - the less accurate the source location will be indicated.

As mentioned, the shape of an array response is a first sensitivity indication. Optimal the array response is a delta function, a small circular lobe, what indicates the same sensitivity over the whole array towards each direction. Unfortunately this is often not the case, Appendix C. Most arrays have a response function in the shape of an ellipse. Due to positioning of the receivers, spacing between them and altitude difference. Due to this ellipse shape the array has a higher sensitivity towards the longer axis of this ellipse.

Since this anomaly seems to attribute a small deviation, in comparison with other anomalies, a correction for ellipse shaped response functions was not made. To fully optimize the trace back cones, a study per array response is needed. This in combination with the bigger anomalies.

A bigger anomaly that was found has to do with the geological structure beneath the array. As described in Chapter 4, a CTBT seismic array has a large inter-receiver spacing. This is necessary due to the large wavelengths, microseisms, it records. When the receivers are positioned close to each other this could lead to missed (non recorded) microseisms, aliasing. Although this large inter-receiver spacing is necessary, it causes some troubles in terms of array sensitivity.

The average inter-receiver spacing of a CTBT seismic array is around two kilometers. Due to these large distances the assumption of a homogeneous subsurface beneath an array is wrong. Each receiver is placed on an unique subsurface. This subsurface structure is only interesting

for body waves, approaching the array from beneath. Although the crust structure beneath the array could be the same, the thickness of these crust layers are different. Since it is to hard to analyze the crust layer structure beneath a receiver, only the Moho depth is of interest. This because the velocity differences around the Moho, mantle to crust boundary, are of a much higher magnitude than the velocity differences between crust layers.

Analyzing Figure 4-3 and Appendix D, it becomes clear that the Moho depth beneath the arrays differs a lot. The Moho depth difference between sub arrays of the NOA array, Figure 4-3 is in some cases 4 km. This large difference of Moho depth results in enormous differences in measured trace velocities. When an event is recorded by an array, the ray paths per receiver differ due to this Moho depth variation. Calculating the Fisher ratio/SNR out of theses recordings, without correcting for the trace velocities, will result in large deviations.

Something that makes this problem even more challenging is the ray path analyses. By knowing the Moho depth beneath a receiver does not mean a correct correction factor is found. Since the signals do not come from right beneath the receivers, but will travel over the array by an angle of incidence, a more complex correction is needed.

Several papers give an approach to find a correction factor for this phenomena, but since none of these papers shows a logical trend, and all of them are based on empirical laws, it is hard to find a right and plausible correction factor. Further research is needed.

Besides the differences in ray paths approaching the array, another assumption is about the ray paths leaving from source. Assumed is that all rays leaving the source travel the same path from crust to mantle, there is no velocity difference created in the early stage of wave propagation. The only difference in velocity is due to array geology, velocity changes at the source location are not considered. To have a high accuracy, a full ray path reconstruction needs to be done with calculating the velocity differences of each path, taking the source location also in considering.

All the shortcomings mentioned above lead to a deviation of the back azimuth. To compensate for this deviation, two different cone generators can be used. The Gauss standard deviation, known as the 68% rule, uses besides the obtained mean back azimuth all traces within the 68% around this mean to reconstruct the cone. This will lead to a very large cone, noise comes from everywhere. To have a more precises cone the mean with its weight is used, Same idea but with less outliers. The disadvantage of this approach is that the cone can have a large deviation due to the array measurements shortcomings described before. If the mean is off, the weight of the mean is also off. The cone will be accurate, in case of positioning around the mean, but due to a missing correction factor for this mean the cone will still pointing to the wrong direction.

Due to all the above, it is clear a correction factor needs to be found for each array. When the case, the weighted mean cone will be the most accurate to reconstruct the trace back cones, in case of noise. For now this weighted mean will lead to results that are off from the truth. This is probably the reason there is no overlap between the arrays in our results.

Near coastal noises

Another interesting result is that the best beam results often do not point near the possible source location. Analyses of the data, Appendix A, shows that most of the processed data are Surface wave.

Especially arrays located near the coast show a large trend of best beam surface waves, while they do not detect any or just a few body waves. By use of several different researches and own observations, one can conclude that the array recordings are dominated by surface waves due to local features. Ocean wave - Coastal interaction, sea currents into the Norwegian Fjords and sea transition of oceanic towards continental plate causes a lot of surface wave ambient noises.

The clean beamform method seems to be the solution for this problem. By cleaning the power spectrum after beamforming more coherent events become visible, instead of only the event with highest coherence. Due to this new information it is possible to filter the near coastal generated surface waves. A more detailed analysis can be done what can be compared with the numerical simulated data. Leading to promising results like Figure 5-7.

Numerical modeling improvements

The goal of this studies is to find the accuracy of CTBT arrays with respect to localization of source locations, it is obvious that any found deviation of result is tried to be explained by errors due to the arrays. But since this numerical approach such leading information it is worth to examine this as well.

Especially because the results of some previous researches ([Kedar et al., 2008]), quite similar research to what is done in this research, shows different results.

[Kedar et al., 2008] showed a comparison between numerical simulated source areas and observed source areas. The conclusions of Kedar's study is based on one particular day, the observed source location is at the same location where a high ocean-ocean wave interaction region is located. A great result that shows a lot of potential.

Although, a more detailed look at her research shows that only two sensors, of many, point towards the storm region. Other sensors point to complete different directions, probably due to local features. It could be that the two sensors, pointing towards the storm region, are a lucky shot and by coincidence have overlap while they point towards a local feature.

This scenario is most likely due to the fact that [Kedar et al., 2008] uses 3-component sensors. These sensors generate a spectra. Out of this spectra it is not possible to distinguish different phases. It is not clear which phase is used to obtain a source region.

Besides the markable differences in observation techniques between [Kedar et al., 2008] and this research, there are also some issues concerning the numerical source calculation. Most important is the that Kedar does not take the Bathemetry into account.

Instead of Bathemetry, [Kedar et al., 2008] uses $[\sigma h/\beta]$. Where h is the height of the water column and β the shear velocity of water. The shear velocity is chosen constant (2800m/s) by [Kedar et al., 2008]. The chosen constant velocity value is the shear velocity of the bed rock and not the shear velocity of the water column, this will lead to an inaccuracy. Smets showed

in his research an improvement on this, by taking the true water column shear velocity. Still, taking the shear velocity as a constant factor will lead to inaccuracies.

Due to the chosen shear velocity the following theory is applicable. [Jensen et al., 2000] showed that when there is coupling between two media and the shear velocity of the second medium is greater the compressional speed of the first medium is to replace for the elastic reflection coefficient with the two-fluid reflection coefficient using the shear speed of the second medium as the compressional speed of an equivalent fluid medium. Meaning only body waves are generated in the deep ocean, neglecting interface waves.

Having the information of [Jensen et al., 2000] the results of the clean beamform method, Figures 5-5 and 5-6, and the thoughts about near-coastal surface waves are confirmed. Deep ocean wave-wave interaction generates body waves that are coupled near this wave-wave interaction region while the surface waves are generated near coastal.

Something contra dictionary with the results of Kedar who assumed the numerical deep ocean model showed surface waves that also were detected by 3-component sensors, concluded based on seismic power spectra.

[Ardhuin and Stutzmann, 2010, Ardhuin and Herbers, 2013] showed an improvement on [Kedar et al., 2008]. Although the comparison was still based on observed spectral data [Gualtieri et al., 2013, Ardhuin et al., 2015].

Recommendation

Besides some promising results shown in this research there are also points that require more research or/and improvement.

- **Observed source location**
  To compare seismic observations with the numerical approach, it is necessary to upgrade the array sensitivity knowledge. It is highly recommended to do more research regarding the SASC files. Without these files the observed data is useless in case of localization. No comparison can be made when the SASC files are not there/complete.

  To obtain a more accurate source location, an analysis with more arrays is required. This research used arrays that are positioned in Europe. Re commanded is to do an analysis with the used arrays plus arrays positioned in America, Greenland or Iceland.

  Besides corrections and adding arrays, also the processing needs to be optimized. This research showed the promising results of the cleaned power spectrum. Although, this was done by trial and error input of parameters. To create a reliable method more research needs to be done focusing on these clean beamform parameters. Suggested to do this with Fisher analysis.

- **Validating source location**
  Besides the comparison between observed seismic source location and simulated source location, the comparison between observed acoustic source location and seismic source location is recommended. Out of previous studies it became clear that the microbaroms do show a large correlation between observed data and simulated data. The obtained source location of the observed microbarms was related to the source area of the simulated data.

- **Bathymetry**
  When all the above is considered, it would be interesting to characterize the source location. On what kind of bathymetry does the water-earth coupling takes place and is there a difference comparing body and surface waves.

- **Simulated source location**
  When all the above is taken into account, the observed data can be used to validate the simulated data. So far only spectral data is used ([Kedar et al., 2008, Ardhuin and Stutzmann, 2010, Gualtieri et al., 2013, Ardhuin et al., 2015] to localize. Only [Obrebski et al., 2013] showed a study where signal phases were distinguished while localizing. But this was done for teleseismic events. This research showed an approach to distinguish phases for non teleseismic events. When this process is optimized it can contribute to optimize the numerical model regarding relation between ocean wave-wave interaction - resonance - bathymetry.

Bibliography

[Moh,] Moho Depth univ. of helsinki. http://www.seismo.helsinki.fi/mohomap. Accessed: 2017-06.

[Kee,] Personal communication tu delft/knmi. http://www.kweemstra.com/. Accessed: 2017-03.

[Ahern et al., 2007] Ahern, T., Casey, R., Barnes, D., Benson, R., Knight, T., and Trabant, C. (2007). Seed reference manual, version 2.4. *IRIS (http://www. iris. edu/software/pqlx/)*.

[Ardhuin et al., 2015] Ardhuin, F., Gualtieri, L., and Stutzmann, E. (2015). How ocean waves rock the earth: Two mechanisms explain microseisms with periods 3 to 300 s. *Geophysical Research Letters*, 42(3):765–772.

[Ardhuin and Herbers, 2013] Ardhuin, F. and Herbers, T. H. (2013). Noise generation in the solid earth, oceans and atmosphere, from nonlinear interacting surface gravity waves in finite depth. *Journal of Fluid Mechanics*, 716:316–348.

[Ardhuin and Stutzmann, 2010] Ardhuin, F. and Stutzmann, E. (2010). On the {Longuet-Higgins Hasselmann} theory for double-frequency microseisms, and practical estimation of seismic noise from ocean wave model results.

[Berteussen, 1974] Berteussen, K. (1974). Norsar location calibrations and time delay corrections. Technical report, DTIC Document.

[Bokelmann, 1995] Bokelmann, G. H. (1995). Azimuth and slowness deviations from the geress regional array. *Bulletin of the Seismological Society of America*, 85(5):1456–1463.

[Bondár et al., 1999] Bondár, I., North, R. G., and Beall, G. (1999). Teleseismic slowness-azimuth station corrections for the international monitoring system seismic network. *Bulletin of the Seismological Society of America*, 89(4):989–1003.

[Borleanu et al., 2008] Borleanu, F., Popa, M., Grecu, B., and Radulian, M. (2008). Azimuth and slowness corrections at burar array estimated from regional events occurred in the mediterranean area. *Romanian Reports in Physics*, 60(4):1137–1149.

[Brekovskikh, 1973] Brekovskikh, L. (1973). Waves in layered media academic, new york, 1960, chap. 1. 31 ba auld. *Acoustic Fields and Waves in Solids*.

[Bromirski et al., 2013] Bromirski, P. D., Stephen, R. A., and Gerstoft, P. (2013). Are deep-ocean-generated surface-wave microseisms observed on land? *Journal of Geophysical Research: Solid Earth*, 118(7):3610–3629.

[Bugeja, 2011] Bugeja, R. (2011). *Crustal Attenuation in the region of the Maltese Islands using Coda Wave Decay*. PhD thesis, University of Malta.

[Carr, 1993] Carr, D. B. (1993). Azimuth estimation capabilities of the arcess regional seismic array. *Bulletin of the Seismological Society of America*, 83(4):1213–1231.

[Dahlman et al., 2009] Dahlman, O., Mykkeltveit, S., and Haak, H. (2009). *Nuclear Test Ban: converting political visions to reality*. Springer Science & Business Media.

[Dana, 1944] Dana, S. W. (1944). The partition of energy among seismic waves reflected and refracted at the earth's core. *Bulletin of the Seismological Society of America*, 34(4):189–197.

[Donn and Rind, 1972] Donn, W. and Rind, D. (1972). Microbaroms and the temperature and wind of the upper atmosphere. *Journal of the Atmospheric Sciences*, 29(1):156–172.

[Euler et al., 2014] Euler, G. G., Wiens, D. A., and Nyblade, A. A. (2014). Evidence for bathymetric control on the distribution of body wave microseism sources from temporary seismic arrays in africa. *Geophysical Journal International*, page ggu105.

[Evers, 2008] Evers, L. G. (2008). *The inaudible symphony: on the detection and source identification of atmospheric infrasound*. PhD thesis, TU Delft, Delft University of Technology.

[Gal et al., 2016] Gal, M., Reading, A., Ellingsen, S., Koper, K., Burlacu, R., and Gibbons, S. (2016). Deconvolution enhanced direction of arrival estimation using one-and three-component seismic arrays applied to ocean induced microseisms. *Geophysical Journal International*, 206(1):345–359.

[Gerstoft and Bromirski, 2016] Gerstoft, P. and Bromirski, P. D. (2016). weather bomb induced seismic signals. *Science*, 353(6302):869–870.

[Gerstoft et al., 2008] Gerstoft, P., Shearer, P. M., Harmon, N., and Zhang, J. (2008). Global p, pp, and pkp wave microseisms observed from distant storms. *Geophysical Research Letters*, 35(23).

[Gualtieri et al., 2013] Gualtieri, L., Stutzmann, E., Capdeville, Y., Ardhuin, F., Schimmel, M., Mangeney, A., and Morelli, A. (2013). Modelling secondary microseismic noise by normal mode summation. *Geophysical Journal International*, 193(3):1732–1745.

[Hao and Zheng, 2009] Hao, C. and Zheng, Z. (2009). Slowness–azimuth corrections of teleseismic events for ims primary arrays in china. *Journal of seismology*, 13(4):437–448.

[Hasselmann, 1963] Hasselmann, K. (1963). A statistical analysis of the generation of microseisms. *Reviews of Geophysics*, 1(2):177–210.

[Hetzer et al., 2010] Hetzer, C. H., Gilbert, K. E., Waxler, R., and Talmadge, C. L. (2010). Generation of microbaroms by deep-ocean hurricanes. In *Infrasound Monitoring for Atmospheric Studies*, pages 249–262. Springer.

[Huang et al., 2013] Huang, G.-J., Bai, C.-Y., and Greenhalgh, S. (2013). A fast and accurate scheme for travel-time computations and ray-path determinations of global seismic phases in a laterally heterogeneous model. *Seismological Research Letters*, 84(3):505–515.

[Jacobeit et al., 2013] Jacobeit, E., Thomas, C., and Vernon, F. (2013). Influence of station topography and moho depth on the mislocation vectors for the kyrgyz broadband seismic network (knet). *Geophysical Journal International*, 193(2):949–959.

[Jensen et al., 2000] Jensen, F. B., Kuperman, W. A., Porter, M. B., and Schmidt, H. (2000). *Computational ocean acoustics*. Springer Science & Business Media.

[Kedar et al., 2008] Kedar, S., Longuet-Higgens, M., and Webb, F. (2008). The origin of deep ocean microseisms in the north atlantic ocean. *Proceedings of The Royal Society*, 464.

[Kinck et al., 1993] Kinck, J., Husebye, E., and Larsson, F. (1993). The moho depth distribution in fennoscandia and the regional tectonic evolution from archean to permian times. *Precambrian Research*, 64(1-4):23–51.

[Landes et al., 2012] Landes, M., Ceranna, L., Le Pichon, A., and Matoza, R. S. (2012). Localization of microbarom sources using the ims infrasound network. *Journal of Geophysical Research: Atmospheres*, 117(D6).

[Longuet-Higgins, 1950] Longuet-Higgins, M. S. (1950). A theory of the origin of microseisms. *Philosophical Transactions of the Royal Society of London A: Mathematical, Physical and Engineering Sciences*, 243(857):1–35.

[Nikulins, 2017] Nikulins, V. (2017). Seismic properties of soil in the eastern baltic sea region based on the horizontal to vertical spectral ratio method. *Estonian Journal of Earth Sciences*, 66(2).

[NORSAR-February-Database, 2017] NORSAR-February-Database (2017). Datbase earthquakes norsar.

[NORSAR-January-Database, 2017] NORSAR-January-Database (2017). Datbase earthquakes norsar.

[Obrebski et al., 2013] Obrebski, M., Ardhuin, F., Stutzmann, E., and Schimmel, M. (2013). Detection of microseismic compressional (p) body waves aided by numerical modeling of oceanic noise sources. *Journal of Geophysical Research: Solid Earth*, 118(8):4312–4324.

[Ottemöller and Midzi, 2003] Ottemöller, L. and Midzi, V. (2003). The crustal structure of norway from inversion of teleseismic receiver functions. *Journal of Seismology*, 7(1):35–48.

[Posmentier, 1967] Posmentier, E. S. (1967). A theory of microbaroms. *Geophysical Journal International*, 13(5):487–501.

[Shearer, 2010] Shearer, P. M. (2010). Introduction to seismology: The wave equation and body waves. *Lecture Notes: http://www. deep-earth. org/2010/Seismo-1-shearer. pdf.*

[Smets,] Smets, Pieter, y. s. *Infrasound and the dynamical stratosphere*. PhD thesis.

[Waxler and Gilbert, 2006] Waxler, R. and Gilbert, K. E. (2006). The radiation of atmospheric microbaroms by ocean waves. *The Journal of the Acoustical Society of America*, 119(5):2651–2664.

[Willis et al., 2004] Willis, M., Garcés, M., Hetzer, C., and Businger, S. (2004). Infrasonic observations of open ocean swells in the pacific: Deciphering the song of the sea. *Geophysical research letters*, 31(19).

[Yang and Ritzwoller, 2008] Yang, Y. and Ritzwoller, M. H. (2008). Characteristics of ambient seismic noise as a source for surface wave tomography. *Geochemistry, Geophysics, Geosystems*, 9(2).

[Zoeppritz and ERDBEBENWELLEN, 1919] Zoeppritz, K. and ERDBEBENWELLEN, V. (1919). Uber reflexion und durchgang seismischer wellen durch unstetigkeits-flachen. *Nachrichten von der Kniglichen Gesellschaft der Wissenschaften zu Gttingen*, 7.

Appendix A

Box plots

A-1 NORSAR

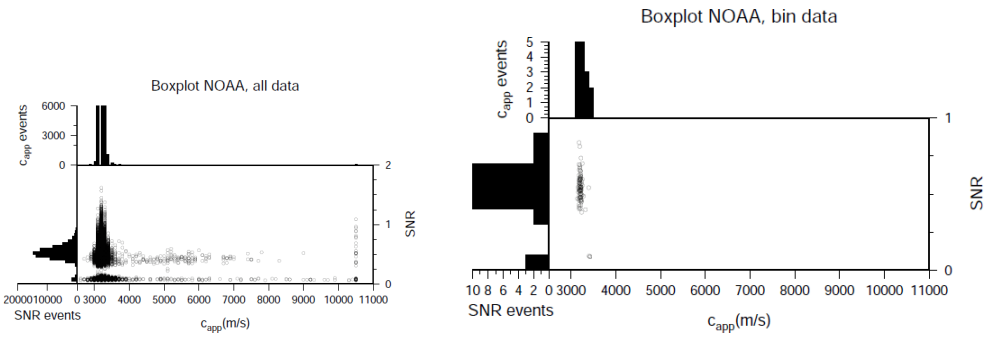

Figure A-1: Boxplot of the NORSAR array, data from 01-01-2017 till 01-03-2017.

A-2 ARCESS

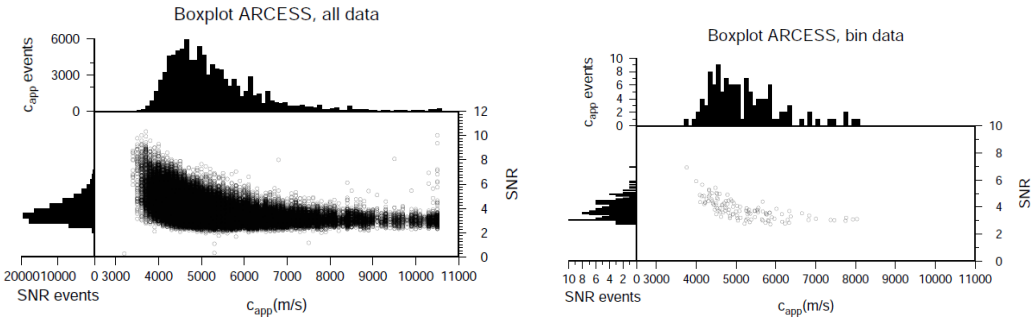

Figure A-2: Boxplot of the ARCESS array, data from 01-01-2017 till 01-03-2017.

A-3 SPITS

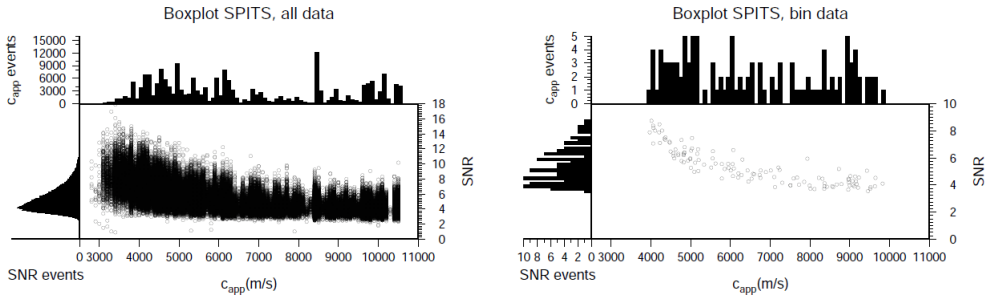

Figure A-3: Boxplot of the SPITS array, data from 01-01-2017 till 01-03-2017.

A-4 AKASG

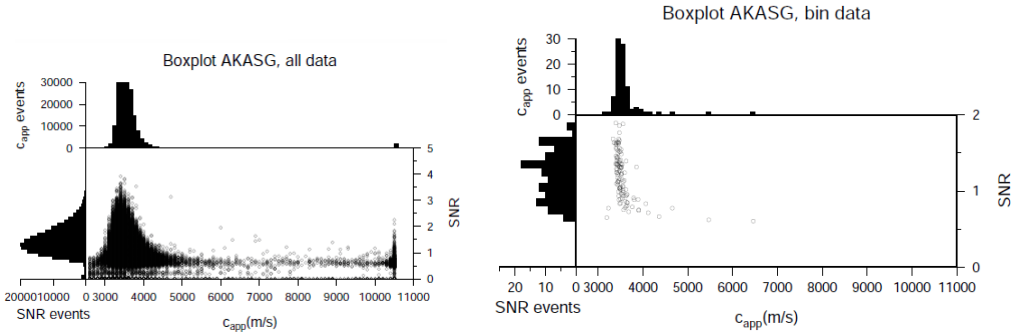

Figure A-4: Boxplot of the AKASG array, data from 01-01-2017 till 01-03-2017.

A-5 ESDC

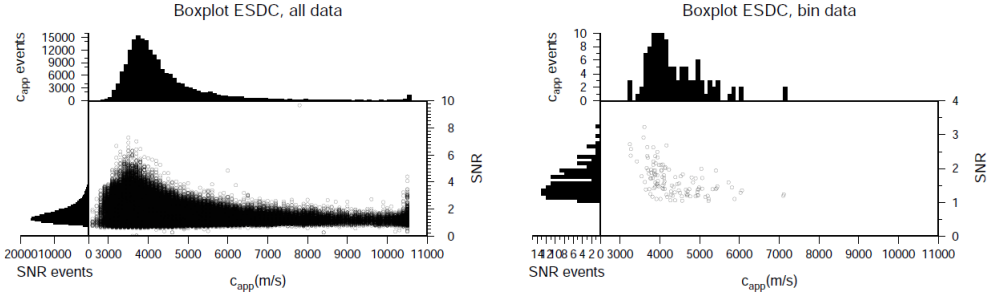

Figure A-5: Boxplot of the ESDC array, data from 01-01-2017 till 01-03-2017.

A-6 GERESS

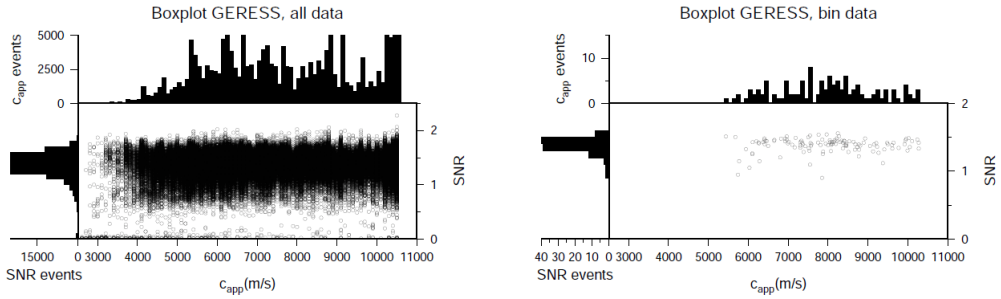

Figure A-6: Boxplot of the GERESS array, data from 01-01-2017 till 01-03-2017.

Appendix B

Processing analysis

B-1 NORSAR and ARCESS

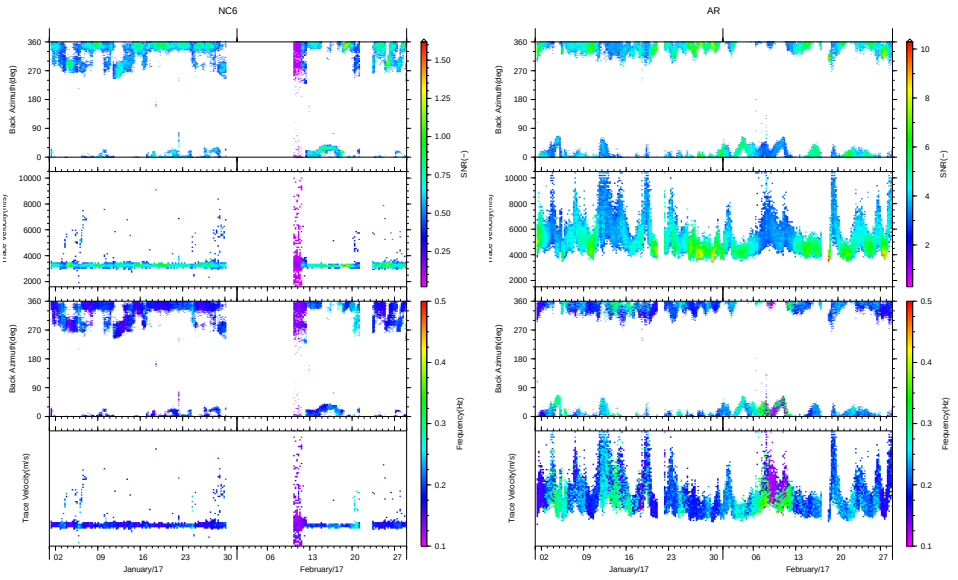

Figure B-1: Processing result NORSAR and ARCESS array, data from 01-01-2017 till 01-03-2017.

B-2 AKASG and SPITS

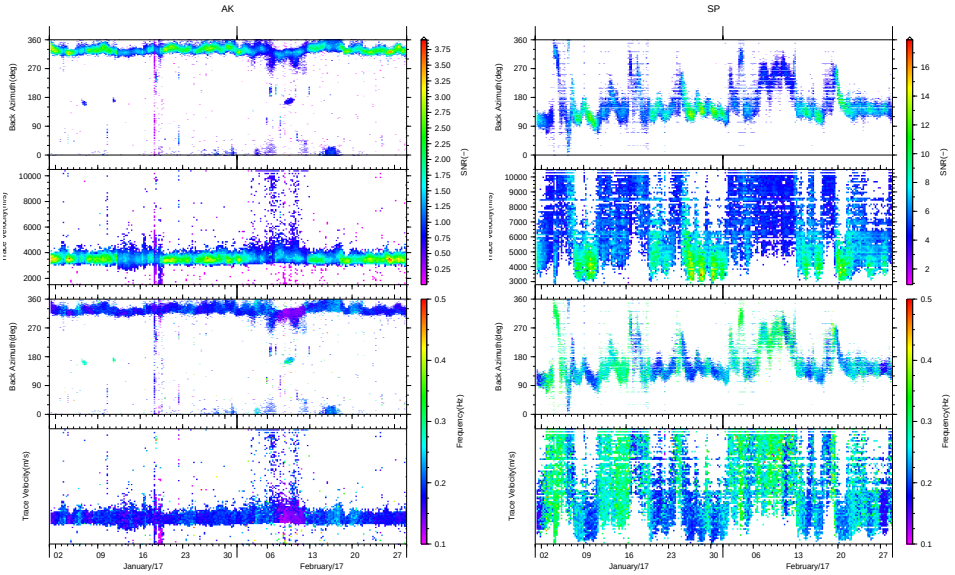

Figure B-2: Processing result AKASG and SPITS array, data from 01-01-2017 till 01-03-2017.

B-3 GERESS and ESDC

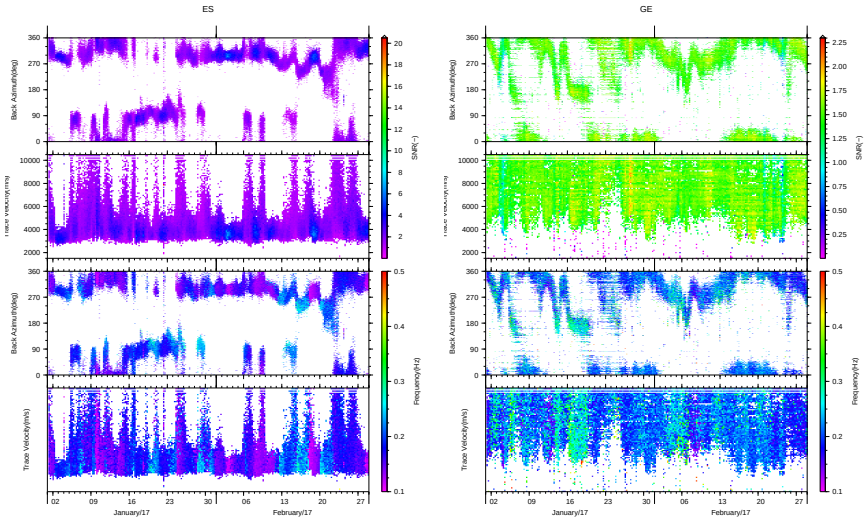

Figure B-3: Processing result GERESS array, data from 01-01-2017 till 01-03-2017.

Appendix C

Array design

C-1 NOA and ARCESS

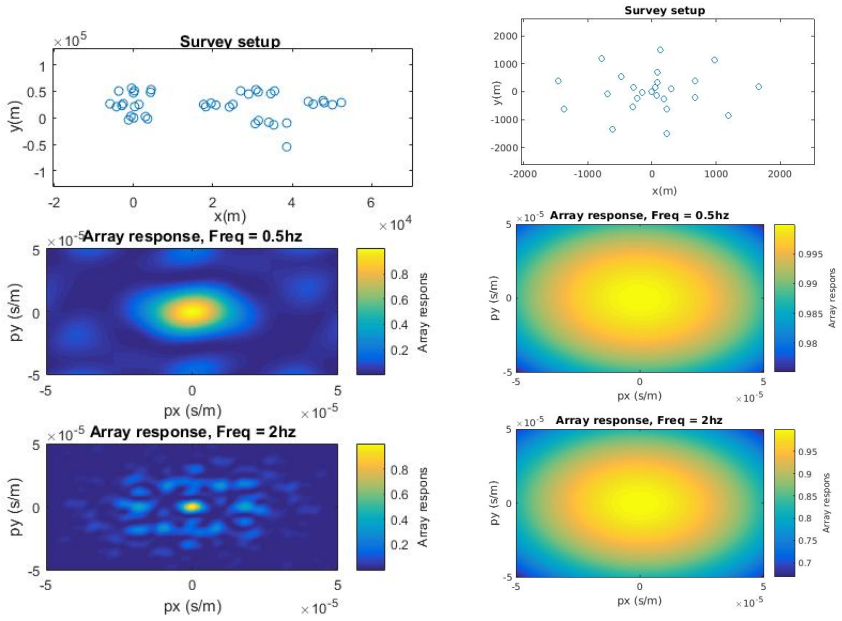

Figure C-1: Array response NORSAR and ARCESS arrays, plane wave from above, P = 0.

C-2 SPITS and AKASG

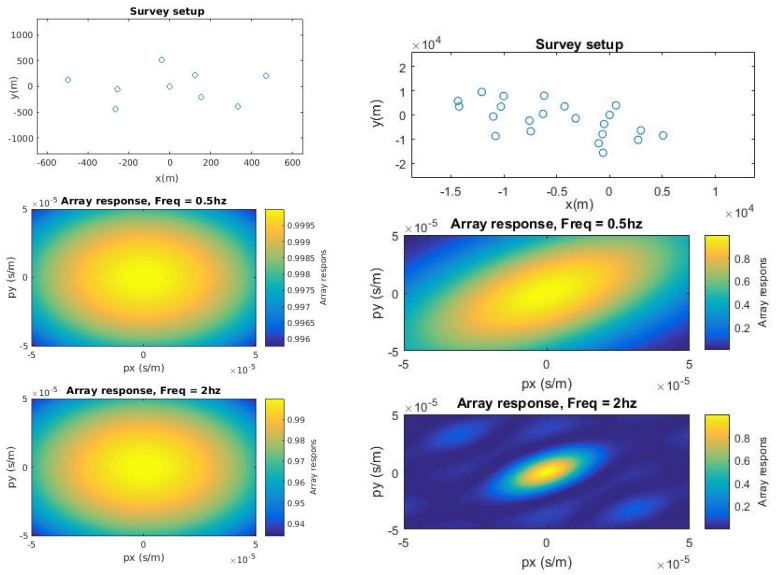

Figure C-2: Array response SPITS and AKASG arrays, plane wave from above, P = 0.

C-3 GERESS and ESDC

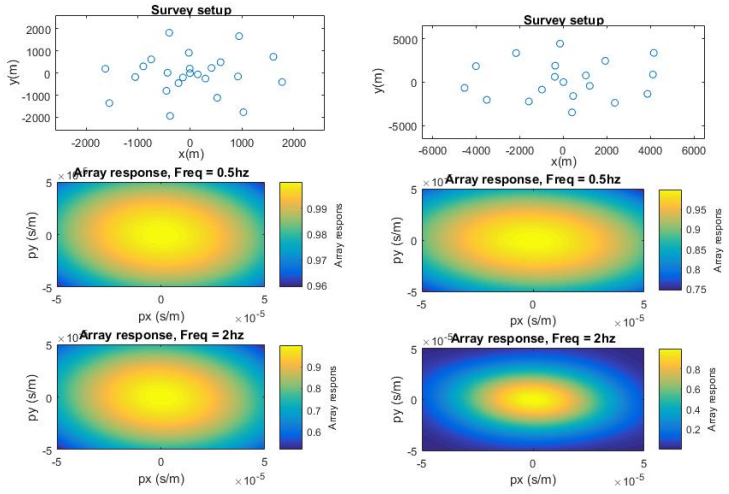

Figure C-3: Array response GERESS and ESDC arrays, plane wave from above, P = 0.

Appendix D

Moho depth

D-1 NORSAR and ARCESS

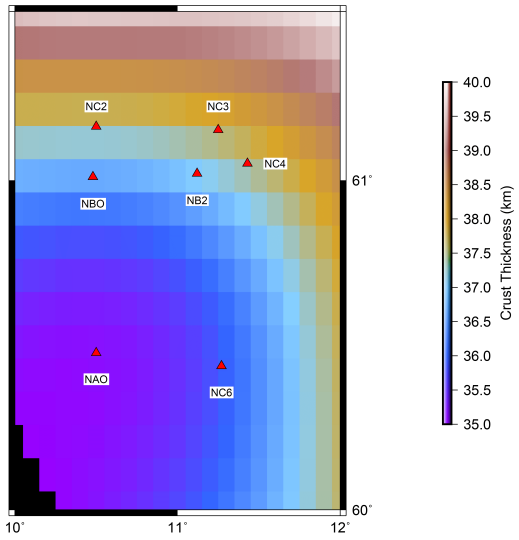

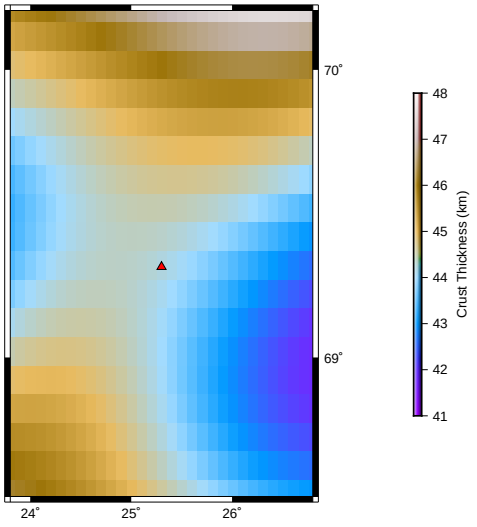

D-2 SPITS and AKASG

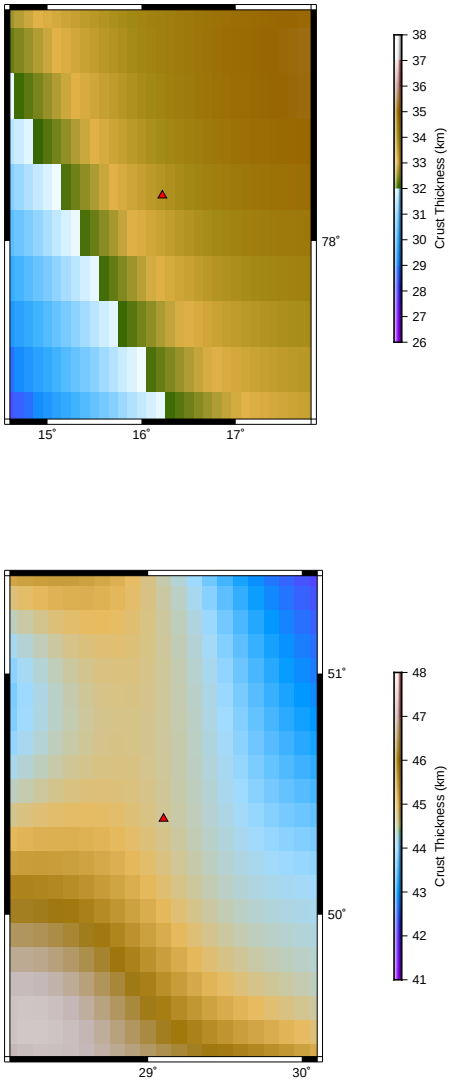

Figure D-2: Moho depth profile beneath SPITS and AKASG arrays

D-3 GERESS and ESDC

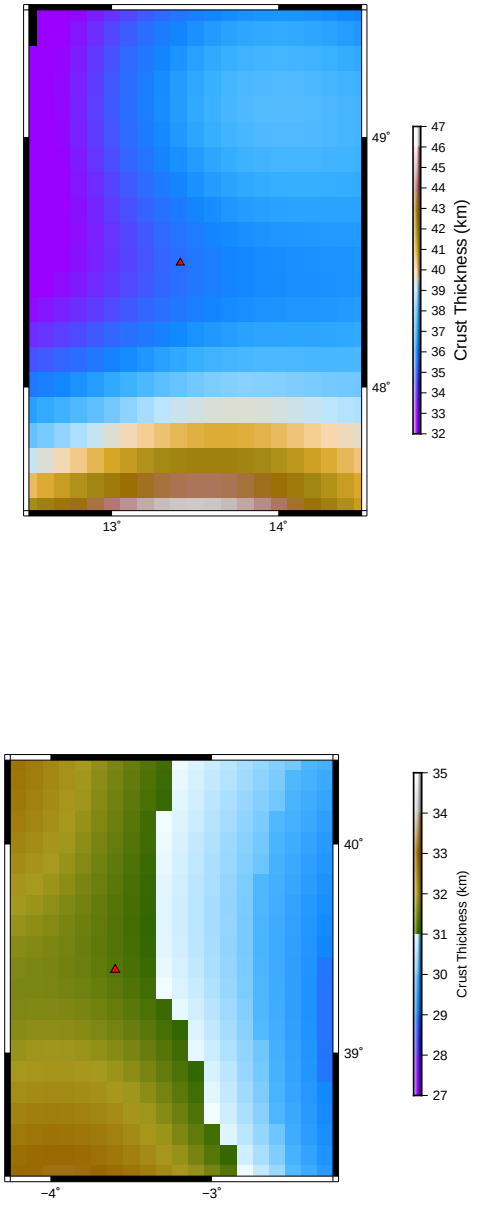

Figure D-3: Moho depth profile beneath GERESS and ESDC arrays

Appendix E

Array Response

E-1 NORSAR and ARCESS

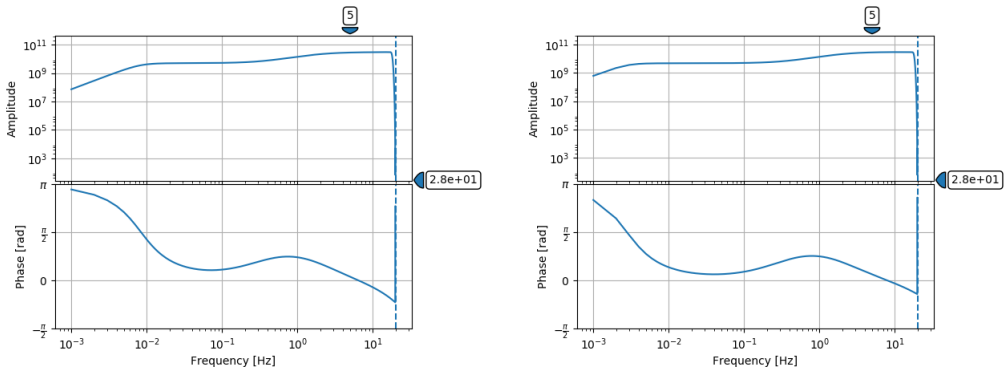

Figure E-1: Station responses of the NORSAR and ARCESS arrays, both BHZ stations.

E-2 ESDC and GERSS

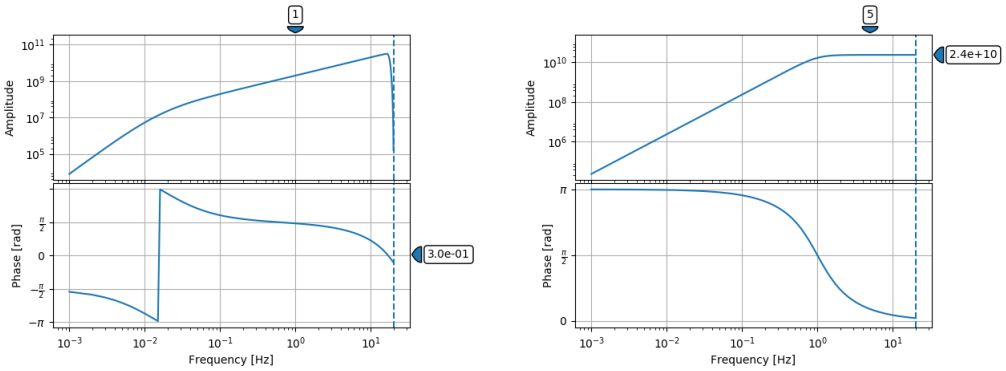

Figure E-2: Station responses of the ESDC(BHZ) and GERESS(SHZ) arrays.